1   This manuscript is submitted for publication in Applied Energy. Please note that, this

2   manuscript has not undergone peer-review and is not yet formally accepted for publication.

3   Subsequent versions of this manuscript may have slightly different content. If accepted, the

4   final version of this manuscript will be available via the 'Peer-reviewed Publication DOI'

5   link on the right-hand side of this webpage.

6

Pore-scale imaging of hydrogen displacement and trapping in porous media

9   *Eike M. Thaysen[1*], Ian B. Butler[1], Aliakbar Hassanpouryouzband[1], Damien Freitas[1],*

10   *Fernando Alvarez-Borges[2], Samuel C. Krevor[3], Niklas Heinemann[1], Robert Atwood[2],*

11   *Katriona Edlmann[1]*

12   [1]School of Geoscience, Grant Institute, The King's Buildings, The University of Edinburgh,

13   James Hutton Road, Edinburgh, EH9 3FE, United Kingdom

14   [2] Diamond Light Source Ltd, Harwell Campus, Didcot OX11 0DE, United Kingdom

15   [3] Department of Earth Science and Engineering, Imperial College London, London SW7
16   2AZ, United Kingdom

17

---

[*] = corresponding author email, phone number: eike.thaysen@ed.ac.uk, +34 682079236

Abstract

Hydrogen can act as an energy store to balance supply and demand in the renewable energy sector. Hydrogen storage in subsurface porous media could deliver high storage capacities but the volume of recoverable hydrogen is unknown. We imaged the displacement and capillary trapping of hydrogen by brine in a Clashach sandstone cylinder at 2-7 MPa pore fluid pressure using X-ray computed microtomography. Hydrogen saturation obtained during drainage at capillary numbers of $<10^{-7}$ was ~50% of the pore volume and independent of the injection pressure. Fluid configuration in the pore space was indicative of a water wetting system at all conditions. Capillary trapping of hydrogen via snap-off during secondary imbibition at a capillary number of 2.4×10^{-6} systematically increased with pressure, 20%, 24% and 43% of the initial hydrogen trapped at 2, 5 and 7 MPa, respectively. Injection of brine at increasing capillary numbers up to 9.4×10^{-6} reduced capillary trapping. Based on these results, we recommend more shallow, lower pressure sites for future hydrogen storage operations in porous media.

Keywords: geological hydrogen storage, μCT, porous media, recovery, drainage, imbibition

Highlights:

- Hydrogen injectivity and recovery in rock is imaged with x-ray computed micro-CT
- Hydrogen recovery decreases with increasing reservoir depth
- Hydrogen recovery increases with increasing brine flow rate
- Hydrogen trapping occurs via snap-off processes
- Nitrogen is a poor proxy for hydrogen

1. Introduction

The storage of surplus electrical energy could increase the utility of renewable energy sources thereby reducing the environmental impact of energy generation[1, 2]. Storage mediums like batteries, compressed air, capacitors, or flywheels are only applicable for the short-term and small-scale electricity storage[3]. The use of hydrogen (H_2) as an energy vector however could provide long-term storage to balance the intermittent demand and supply challenges affecting renewable methods[3]. Considering the low energy density of H_2[4], storage of H_2 in large storage sites is the only solution for economical, gigawatt to terawatt-scale H_2 storage. Underground storage of H_2 in salt caverns is an established technology[5], yet, only subsurface porous media (saline aquifers and depleted oil and gas fields), can provide TWh storage capacities that could balance seasonal demands[4]. Relative to cavern storage, inter-seasonal storage in porous media is poorly understood and introduces a range of other complexities[2], including potential pore-clogging by microbial growth[6], gas loss out of diffuse lateral boundaries, viscous fingering of H_2 into reservoir brines, residual trapping and possible reactions with the primary formation fluid and reservoir minerals[7-10]. Each of these requires consideration of multiphase flow, transport and reaction[2, 8].

Recent years have seen several studies on H_2 geochemistry[11-13] and the elucidation of many important flow characteristics of H_2 including; Hydrogen relative permeability[14, 15], interfacial tension (IFT)[16, 17], and H_2/brine/rock contact angles[14, 16-24]. Yet, additional data describing the H_2 fluid flow in different porous formations and under varying conditions are vital to make accurate predictions of the H_2 plume development and to define optimum production strategies[8]. Of particular relevance is the degree of capillary trapping, which leads to a reduced volume of recoverable H_2, in this way impacting the economic feasibility of the operation[8]. The capillary forces that control capillary trapping also control the relative permeability[8]. As such

66 studies on residual trapping give insight to a range of crucial input parameters for pore-scale

67 and reservoir H_2 storage models.

68 The effects of the brine pore fluid pressures and of brine flow rate on capillary trapping of H_2

69 are hithertho unknown. The brine pore fluid pressure is linked to the reservoir depth via the

70 hydrostatic gradient, hence an investigation of the latter could facilitate the definition of an

71 optimal storage depth for gas recovery. The flowrate affects the capillary number, N_c, via

72 equation 1:

73 $$N_C = \frac{q \cdot \mu}{\sigma} \tag{1}$$

74 where q is the flow, μ is the viscosity and σ is the interfacial tension (IFT). As N_c increases,

75 viscous forces dominate capillary forces and capillary trapping of the nonwetting phase

76 decreases[25]. This capillary desaturation with increasing N_c, depends on the rock type[26] and on

77 the kind of nonwetting phase[25] and is observed around critical capillary numbers of 10^{-5} to 10^{-}

78 ^{8} [25].

79 A non-destructive standard technique for visualization and analysis of wetting and non-wetting

80 phase displacement processes in porous media is x-ray micro-computed tomography (μCT)[27].

81 Pore-scale models are directly reliant on μCT images to build up the basic models for

82 appropriate understanding of gas storage operations[28]. Previously published μCT studies on

83 two-phase flow in porous media involving gas have largely focused on supercritical carbon

84 dioxide (sCO_2) in sandstones and limestones, e.g.[27, 29-34]. Reported saturations of sCO_2 in non-

85 aged (i.e. not wettability altered by exposure to oil or organic acids) water-wet rocks range

86 from 30-60% during drainage and 15-30% during imbibition, at N_{Ca} between 10^{-8} to 10^{-6} and

87 10^{-8} to 2×10^{-5}, respectively[27, 30, 32-34]. Studies using subcritical, gaseous carbon dioxide (CO_2),

88 which could be more readily compared to H_2, are scarce. Yet, the characteristic trapping curves

89 for sCO_2 and CO_2, which show the residual saturation (S_{nnwr}) as a function of initial saturation

90 (S_{nwi}), are not significantly different[35]. Saturations of nitrogen (N_2) during drainage and

imbibition in sandstones with 6-22% porosity is 43-64% and 43%, respectively, at N_C between

1-7x10^{-8} [36, 37]. Carbon dioxide trapping increases at lower pressures due to decreasing water

contact angles[38]. Unlike in CO_2 storage, trapping is not desirable in geological H_2 storage as it

leads to unrecoverable H_2.

Some observational studies have suggested that H_2 is less wetting on rocks than CO_2[19, 21]. At

the time of writing two μCT studies, one micro-model study and one nuclear magnetic

resonance (NMR) study on H_2 exist: Al-Yaseri et al. (2022)[39] used NMR to find H_2 S_{nwi} and

S_{nwr} of 4% and <2%, respectively, in a Fontainebleau sandstone at 0.4 MPa and ambient

temperature. Higgs et al. (2021)[16] μCT-imaged H_2 injection into a 5 mm diameter and 7.6 mm

length core of Bentheimer sandstone at pressures of 6.8 to 20.8 MPa and documented

decreasing IFT between H_2 and water with increasing pressure (72.5 mN/m at 6.9 MPa to 69.4

mN/m at 20.7 MPa). Jha et al. (2021)[40] conducted a single cycle H_2-brine displacement

sequence in a 5 mm diameter and 15 mm length Gosford sandstone, and used μCT to calculate

an S_{nwi} of 65% during drainage and a S_{nnwr} of 41% after brine imbibition. Rock samples in Jha

et al. (2021)[40] and Higgs et al. (2021)[16] were sufficiently short for capillary end effects to

dominate the flow behaviour, where the wetting phase accumulates close to the production face

of the core[41]. The experiment by Jha et al. (2021)[40] was performed at ambient pressure and

leaves open the question of variations in H_2 wetting and flow behaviour at reservoir

conditions[19]. Increasing pore fluid pressures have been reported to increase the gas saturation

and pore network connectivity for nitrogen (N_2) in a brine wet, aged Bashijiqike tight sandstone

(0.6% gas saturation at 2 MPa versus 43% at 8 MPa)[36]. The effect of N_C increases from 7.7x10^{-7} to 3.8x10^{-4} on the H_2 flow through a sandstone micro-model at 0.5 MPa was investigated by

Lysyy et al. (2022)[20] who found that H_2 saturation increased correspondingly from 18% to

79%[20].

115 In this work, we used μCT to investigate the displacement and capillary trapping of H_2 by brine

116 in 4.7 mm diameter and 54-57 mm length Clashach sandstone cores as a function of gas and

117 brine pore fluid pressure (2-7 MPa) and flow rate (20 to 80 μl min^{-1}, corresponding to H_2 and

118 brine bulk N_C of 1.7-6.8x10^{-8} and 1.2-9.4x10^{-6}, respectively). We show that the H_2 S_{nwi} is

119 independent of pore fluid pressure but that higher brine pore fluid pressures during secondary

120 imbibition increase capillary trapping of H_2, indicating increased trapping at elevated reservoir

121 depths. Higher flowrates during secondary imbibition on the other hand decrease capillary

122 trapping. Our work advances the current understanding of H_2 flow in porous media by

123 delivering the first realistic estimates on how much H_2 can be recovered from the subsurface

124 after injection, disregarding any H_2 loss by microbial or geochemical reactions, as a function

125 of reservoir depth and flow rate.

126

127 **2. Materials and Methods**

128 *2.1 Core-flooding experiments*

129 We performed non-steady and steady state, two-phase core flooding experiments with H_2

130 (purity 99.9995 vol.%, BOC Ltd.) and brine (0.5 M CsCl or 2 M KI, Sigma-Aldrich) in a

131 Clashash sandstone (Permian, Aeolian sandstone from near Elgin in Scotland. Clashach

132 composition: ~96 wt.% quartz, 2% K-feldspar, 1% calcite, 1% ankerite[42], porosity 11.1-

133 14.4%[42-44]) at ambient temperature (~293 K). The Clashach sandstone, with its low

134 mineralogical variability, yet still comparably big pore space, was chosen in order to facilitate

135 the visualization of the injected H_2 and the interpretation of the results.

136 Two types of experiments were carried out: The first set of experiments (from now on referred

137 to as UoE (Univeristy of Edinburgh) experiments) was carried out using the μCT instrument

138 at the University of Edinburgh and were aimed at imaging the displacement and capillary

139   trapping of H_2 by brine as a function of saturation after drainage and imbibition under different

140   experimental conditions. Three UoE experiments were carried out that investigated the effect

141   of injection pressure (2-7 MPa), whereof each was repeated once (UoE exp. 1-3, Table 1). The

142   standard error on the H_2 saturation in the repeated experiments was calculated as the standard

143   deviation devided by the square root of the number of repeated experiments. One UoE

144   experiment looked at the effect of the H_2/brine injection ratio on the H_2 saturation (UoE exp.

145   4, Table 1). This experiment was carried out to evaluate the effect of H_2 injection into aquifers

146   with different magnitudes of brine flow (hydrodynamic aquifers), and to simulate the far field

147   situation, where H_2 and brine move together. Another UoE experiment investigated the effect

148   of secondary drainage and imbibition (UoE exp. 5, Table 1). UoE exp. 6 used N_2 instead of H_2.

149   This experiment was undertaken in order to compare the flow behaviour of the two gases,

150   which is of relevance because N_2 is sometimes used as an analogue for H_2, e.g. in permeability

151   measurements[11, 15]. Because rearrangement processes in the pore volume were noted previously

152   for N_2[36], UoE exp. 7 (Table 1) was undertaken to examine the stability of H_2 in the rock volume

153   over an experimental duration (10 hours): Ten PV of H_2 were injected into a brine-saturated

154   rock and keeping the pressure constant inside the pressure vessel, with imaging undertaken at

155   the start and after 10 hours. The effect of bulk capillary number on drainage and imbibition

156   was deduced by a comparison of the results from UoE exp. 2 and 5 which used flowrates of 20

157   and 80 µl min^{-1}, respectively, and 5 MPa injection pressure (Table 1).

158   The second type of experiment (from now on referred to as the 'dry rock experiment'; Table

159   1) used synchrotron radiation (Diamond Light Source, I12-JEEP tomography beamline) to

160   capture the time-resolved displacement of H_2 by brine in a dry, H_2-saturated rock. This

161   experiment served as a base of comparison to the displacements of H_2 in wet, brine-saturated

162   rock (UoE experiments).

163   All experiments used a bespoke x-ray transparent core holder for a 5 mm diameter rock core,

164   **Table 1: Overview over experiments**

Experiment	Type of x-ray source	Description	Sample	H$_2$/brine injection ratio(s)	Flowrate (μl min^{-1})	Injection Pressure (MPa)	Confining Pressure (MPa)	Pore volumes injected	Repetitions of experiment
UoE exp. 1	laboratory	Primary drainage and imbibition in non-steady state displacements of H$_2$ and brine	1	-	20	7	9	10	1 entire repetition, 1 repetition on drainage only
UoE exp. 2	laboratory	Primary drainage and imbibition in non-steady state displacements of H$_2$ and brine	1	-	20	5	9	10	1
UoE exp. 3	laboratory	Primary drainage and imbibition in non-steady state displacements of H$_2$ and brine	1	-	20	2	9	10	1
UoE exp. 4	laboratory	Simultaneous, steady state injections of H$_2$ and brine	1	1:4, 1:1, 4:1	20	5	9	10	-
UoE exp. 5	laboratory	Primary and secondary drainage and imbibition in non-steady state displacements of H$_2$ and brine	1	-	80	5	9	10	-
UoE exp.6	laboratory	Non-steady state displacements of N$_2$ and brine	1	-	20	5	9	10	-
UoE exp.7	laboratory	H$_2$ stability	1	-	80	5	9	10	-
Dry rock	synchrotron	Non-steady state, brine injection into dry, H$_2$ saturated rock	2	-	5	5	10	10	-

165

166   which was a scaled-up version of the cell described by Fusseis et al. (2014)[45]. In UoE

167   experiments a carbon-fibre reinforced PEEK pressure vessel was used to permit good x-ray

168   transparency. The dry rock experiment used an aluminium pressure vessel to comply with the

169   health and safety requirements at Diamond Light Source. The specifications of the pressure

170   vessels of PEEK and aluminium were engineered with safety factors of 2 times or more over

171   and above the maximum applied confining pressure (10 MPa; Table 1).

172   Rock cores for the experiments were obtained by diamond drill coring with a water-flushed

173   chuck, followed by preparation of the core ends by grinding on a lathe. Experiments used a set

174   of four high-pressure pumps (Cetoni Nemesys^{TM}, flowrate range 0.072 nl s^{-1} to 13.76 ml s^{-1}):

175   One for the injection of H_2, one for the injection of brine, one to hold the backpressure and one

176   for the confining pressure (Fig. 1). A bespoke manifold system composed of high-pressure 1/8"

177   and 1/16" 316 stainless steel and 1/16" PEEK tubing (Swagelok, Top Industrie and Cole

178   Parmer, respectively) connected the pumps to the core-flood cell (Fig. 1). Additional pressure

179   transducers (ESI Technology; accuracy 0.1% full-scale) were coupled to the flow system at the

180   inlet and outlet to allow for higher precision pressure monitoring than was possible using the

181   integral pressure gauges in the syringe pumps. Cyclic H_2 and brine injections used a Clashach

182   outcrop sample without further cleaning of 4.7 mm diameter and a relatively long length of 54-

183   57 mm to avoid the influences of capillary end effects[46, 47]. To prevent leakage of H_2 into the

184   confining fluid, the rocks were jacketed in aluminium foil and poluolefin heatshrink tubing and

185   sealed with silicone adhesive between the conical-ended pistons within the pressure vessel. In

186   UoE experiments, a water-wet rock was first saturated with brine (0.5 M CsCl) at a flow rate

187   of 70 μl min^{-1}. Afterwards, H_2 was injected (drainage) into the brine-saturated rock at flow

188   rates of 20-80 μl min^{-1}, based on desired capillary-regime N_C of 1.7-6.8x10^{-8} (The viscosity of

189   H_2 is 9.01 μPa s at 298K and 4.7 MPa[48] and the IFT between H_2 and water is 72.6 mN m^{-1} at

190   298K and 5 MPa[49, 50]). Subsequently, the brine was reinjected (imbibition) at flow rates of 20-
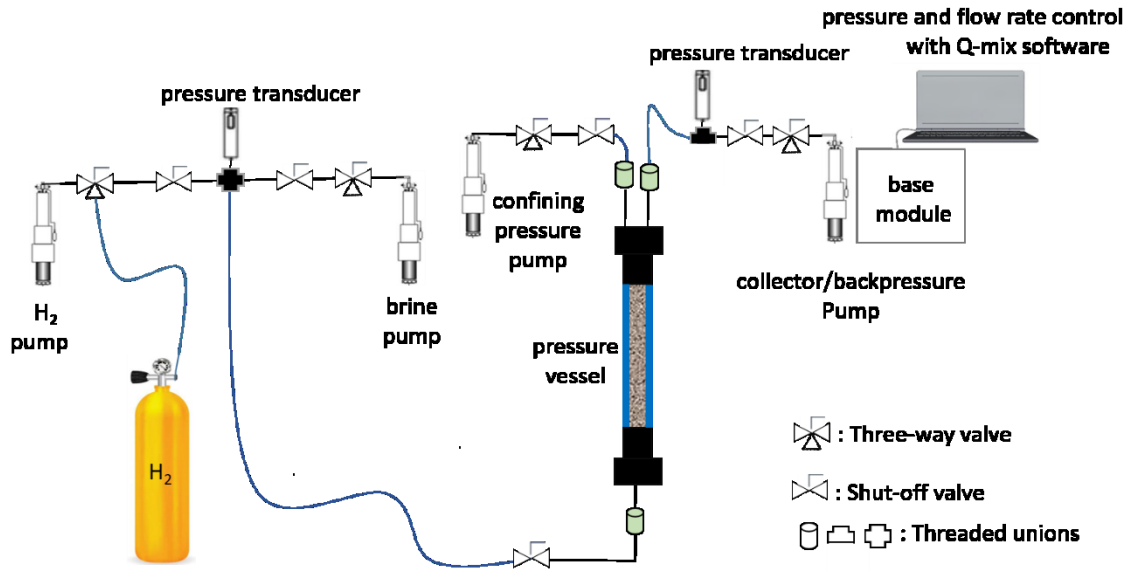
Figure 1: Experimental setup showing the manifold system that connected the X-ray transparent pressure vessel to a set of four high-pressure Cetoni Nemesys[TM] pumps: one to inject H_2, one inject brine, one to maintain backpressure and one to maintain confining pressure. The materials for the connections were 316 stainless steel (black), HPLC (green) and PEEK or carbon fibre reinforced PEEK (blue). The pressure vessel consisted of carbon fibre reinforced PEEK in UoE experiments and of aluminium in the dry rock experiment (see text). Pressure and flow rate control was achieved with the Q-mix software.

191

192   80 µl min^{-1}, resulting in N_C of 2.35-9.45x10^{-6} (using the same IFT between H_2 and water of

193   72.6 mN m^{-1} at 5 MPa and 298 K[49, 50] and a viscosity of 1.247 Pa s at 5 MPa that was estimated

194   from the reported 1.2503 Pa s and 1.233x10^{-3} Pa s at 0.1 MPa and 25 MPa, respectively, and

195   298 K[51]). The N_C the N_2 experiment was 3.5x10^{-8} (using an IFT of 73 mN m^{-1} between N_2 and

196   water 1t 298K and 10 MPa[35] and a viscosity of 1.89x10^{-5}Pa s at 5 MPa and 295K[48]). Each

197   injection used ten pore volumes to ensure completely flushing of the sample cores with the

198   injected fluid.

199   In the dry rock experiment, H_2 was directly injected into a dry rock at a flow rate of 70 µl min^{-}

200   ^{1}. Subsequently, the brine (2 M KI) was injected at a flow rate of 5 µl min^{-1}, resulting in N_C of

201   5x10^{-7} (using the same IFT between H_2 and water of 72.6 mN m^{-1} at 5 MPa and 298 K[49, 50] and

202   a viscosity of 1.07x10^{-3}Pa s for 0.6 M KI and 293 K[42]).

203 The combined application of an x-ray transparent core holder and μCT allowed the

204 visualization of the fluid saturation distributions at pore scale at each injection step. The

205 difference in the x-ray attenuation coefficient of the fluids (H_2 and 0.5 M CsCl/ 2 M KI)

206 provided an excellent contrast between the two fluid phases and the rock on the acquired μCT

207 images, combined with the respective radiation energy in the two different laboratories.

208 3D volumes were acquired from the lower central portion of the sample to avoid the impact of

209 capillary end effects on fluid saturation[46, 47]. For the UoE experiments, image acquisition used

210 a μCT instrument built in-house at the University of Edinburgh, comprising a Feinfocus 10-

211 160 kV reflection source, a Micos UPR-160-air rotary table and a Perkin-Elmer XRD 0822 1

212 MP amorphous silicon flat panel detector with a terbium doped gadolinium oxysulfide

213 scintillator. Data acquisition software was developed in-house. The following settings were

214 used for UoE experiments: 120 keV, 16 W, 2 seconds exposure time, 1200 projections and 2

215 frames per stop. The voxel size was 5.4 μm^3. In the dry rock experiment, time-resolved imaging

216 of the H_2 and brine displacement processes was achieved by means of a 65 keV monochromatic

217 beam detected by a high-resolution imaging camera with optical module 2 (PCO.edge 5.5, 7.91

218 x 7.9 μm/pixel with FoV 20 mm x 12 mm) using 17-25 milliseconds exposure time and 900

219 projections. The voxel size was 7.9 μm^3.

220 *2.2 Image analysis*

221 Tomographic reconstructions were undertaken by filtered back projection using Octopus 8.9[52]

222 on a GPU accelerated workstation. All subsequent image processing and analysis of

223 tomographic data was performed using Avizo Version 9.1.1 (FEI, Oregon, USA). Data from

224 UoE experiments were processed using a non-local means filter[53]. Processing of the dry rock

225 experiment used a combination of median filter and unsharp mask to reduce image

226 noise.Segmentation of UoE experiment data used a global threshold on the 2D greyscale image

227 histogram, and encompassed two phases. In the water-saturated scans, water and rock were

228 treated as two discrete phases. In scans after brine and H_2 injections, the H_2 was treated as one

229 phase and the brine and rock as a single separate phase, following protocols of Andrew et al.

230 (2014)[32]. Holes and spots which were at the resolution limit of the data were removed from all

231 datasets (applied thresholds corresponded to 3^3 and 5^3 voxels, respectively). Based on the

232 segmented image of the water-saturated scan in UoE experiments, a pore size distribution was

233 calculated. The 3D image was separated into individual pores and throats using Avizo's

234 'separate objects' module, which calculates a chamfer distance map of the pore-space and then

235 applies a marker based watershed algorithm to the distance map to define discrete pore bodies

236 as catchment basins separated by the watershed which marks the location of pore throats (SI

237 Figure S1d). Supporting information Figure S1 shows the work flow for the water-saturated

238 scan.

239 In scans following brine and H_2 injections in UoE experiments, the segmented image was

240 analysed in 3D using the 'labeling' and 'label analysis' modules to identify, label and measure

241 the volume of each H_2 cluster. Hydrogen cluster size distributions were compared to the pore

242 size distribution to evaluate the H_2 connectivity and identify trapping mechanisms during brine

243 imbibition.

2.3 Capillary pressure

245 Recovered Clashach cores were submerged in 25% w/v NaOH solution (Fisher Scientific) for

246 2 hours to remove the aluminium foil from the core surface, and rinsed in successive milli-Q

247 water, acetone and ethanol ultrasonic baths. Subsequently, the cores were cut and squared to

248 the dimensions of 25 mm, overlapping the μCT visualized rock volumes, and cleaned

249 ultrasonically with milli-Q water to remove grinding products. Mercury injection capillary

250 pressure (MICP) was performed on the cleaned cores, using a micromeritics automated

251 mercury injection equipment (Autopore IV 9500) to estimate the capillary pressure-saturation

252 relationship and pore size distribution. The pressure range tested was from vacuum to 379 MPa.

3. Results

3.1 Characterization of the pore space

The μCT-evaluated porosity of the Clashach sandstone from the segmented volume of the water-saturated rock was 12.5% to 13.5%, depending on the imaged region of the rock core. The MICP-evaluated pore throat size distribution showed a large number of very small pore throats with <5 μm radius and a small number of small to intermediate size pore

Fig. 2. μCT-derived pore size distribution (grey) and MICP-derived pore throat size distribution (transparent blue). Note that MICP derived counts were multiplied by a factor of 20 to facilitate visualization of the results. All plots used a bin size of 30.

throats (>5 to 90 μm) (Fig. 2). The largest pore throat had a radius of 195 μm (Fig. 2). The μCT-evaluated size distribution of the pores evidenced a narrow pore size distribution with comparably small pores with radii <50 μm (Fig. 2, 4a).

3.2 Hydrogen wetting behaviour and stability in UoE experiments

Hydrogen sat in the centre of the pore bodies. Residual brine sat in corners, pore throats (Fig. 3b and c) and, as a subtraction of the water saturated scan from the H_2-and brine filled rock revealed, in thin films around the grains (Fig. 3d). The injected H_2 remained stable within the pore volume under no-flow conditions and at constant pore fluid pressure over a time period of 10 hours which was the maximum experimental duration (SI Fig. S2).

3.2 Effect of pore fluid pressure on hydrogen connectivity, saturation and recovery

Hydrogen saturation during drainage was independent of the pore fluid pressure with 49.8%, 51.7% and 39.7%-52.6% saturation at pore fluid pressures of 2, 5 and 7 MPa, respectively (Fig. 4a-c, f, SI Fig. S3). Hydrogen connectivity during drainage generally showed one large,
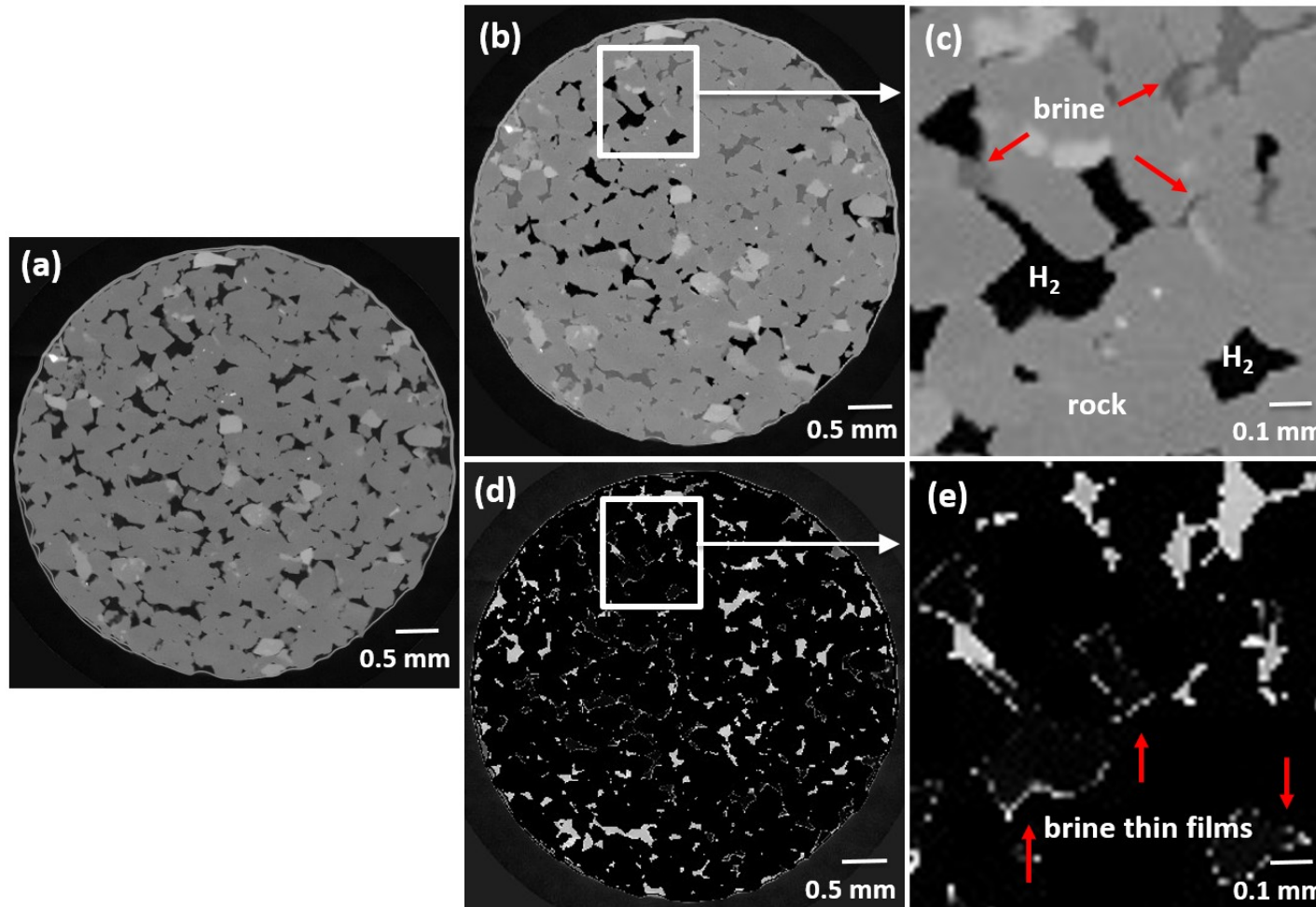
Fig. 3: **(a)** Water-saturated Clashach sandstone with the water shown in black and the rock in different shades of grey. **(b)** and **(c)** Brine-saturated Clashash sandstone after injection of H_2. H_2 (black) fills the centre of the pores while the brine (dark grey) remains in corners and small pore throats around grains. **(d)** and **(e)** Subtraction of the water-wet scan from the brine-saturated scan after H_2 injection, following registration of the brine-saturated scan after H_2 injection to the water-saturated scan, revealing discontinuous brine thin films around grains. The rim around the Al foil in **(d)** is caused by continued shrinkage of the Al foil onto the rock during the experiments.
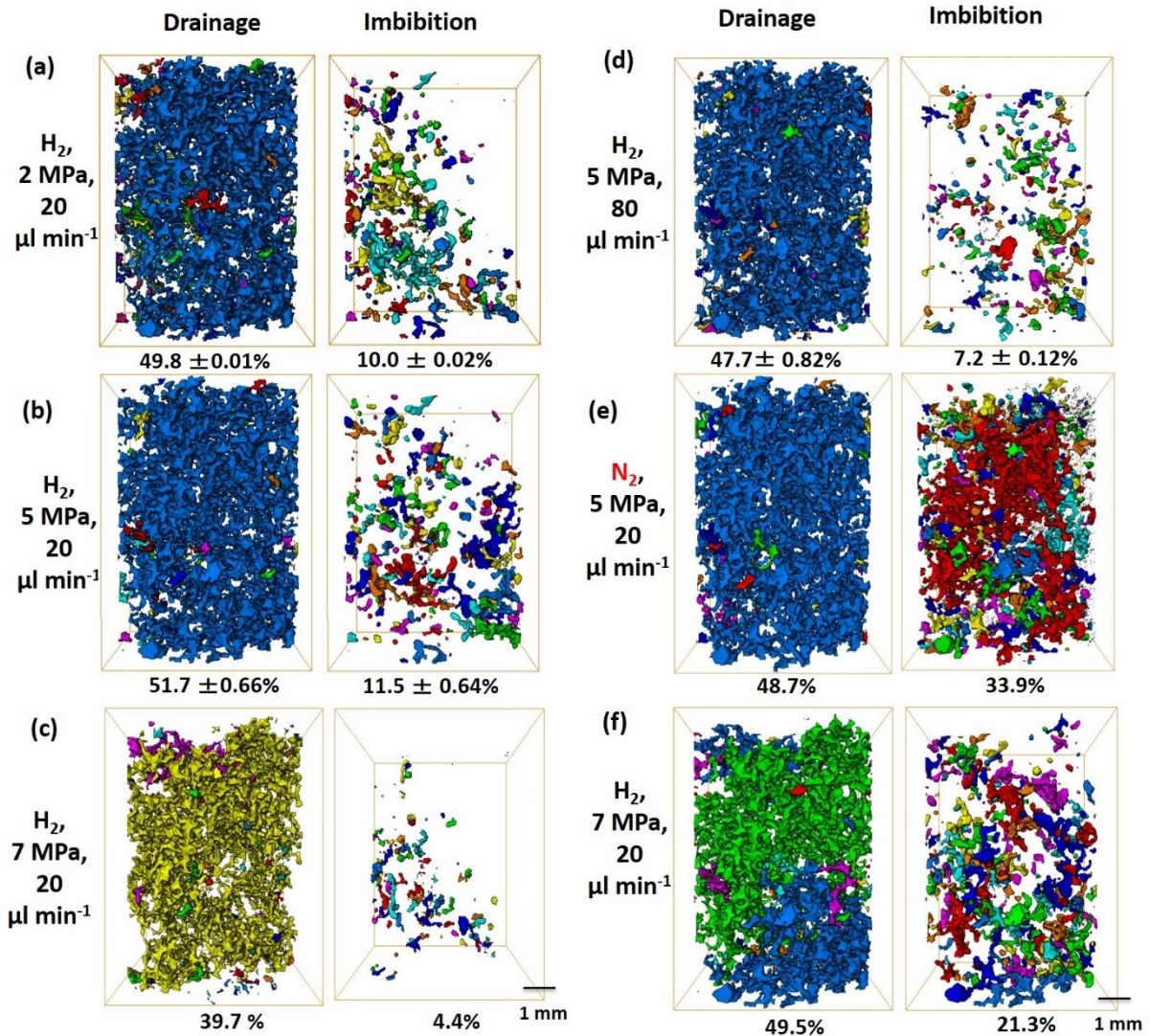
Fig. 4: 3D rendering of H_2 and N_2 clusters with saturation percentages in UoE experiments. Discrete clusters were rendered in colours, where mainly one color marks one large, connected cluster and different colors indicate several, not connected clusters. **(a-c)** Effect of pore fluid pressure on H_2 clusters and saturation after drainage and after primary imbibition. **(a)** 2 MPa, **(b)** 5 MPa and **(c, f)** 7 MPa, all at a constant flow rate of 20 µl min^{-1} corresponding to capillary numbers of 1.7×10^{-8} and 2.4×10^{-6}, respectively. Large, connected clusters that existed after drainage were broken down to numerous smaller clusters after imbibition, with apparently no clear relationship between H_2 saturation and pore fluid pressure. Experiments were repeated once at 2 and MPa, and at 7 MPa twice for drainage runs and once for imbition. For experiments at 2 MPa and 5 MPa averages and standard errors for the H_2 saturation are reported. For experiments at 7 MPa, due to the discrepancy in the results, both of the full primary drainage and imbibition experiments are visualized in **(c)** and **(f)**. **(d)** Effect of cyclic injections on H_2 clusters and saturation: Averages and standard errors of the H_2 saturation after primary and secondary drainage, and after primary and secondary imbibition, all at 5 MPa pore fluid pressure and a flowrate of 80 µl min^{-1} corresponding to a capillary number of 9.4×10^{-6}. **(e)** Nitrogen clusters and saturations during drainage and imbibition at 5 MPa pore fluid pressure and a flowrate of 20 µl min^{-1}. For the full display of the results see SI Fig. S3 and SI Fig S4.

298   connected cluster at all pore fluid pressures except for one out of three images at 7 MPa which

299   showed three large disconnected clusters (Fig. 5, SI Fig. S3). During drainage, the largest H_2

300   cluster had a volume of 1×10^8 μm^3 at all pore fluid pressures except for the one run at 7 MPa

301   with the disconnected clusters were the largest volume was 7×10^7 μm^3 (Fig. 5e).

302
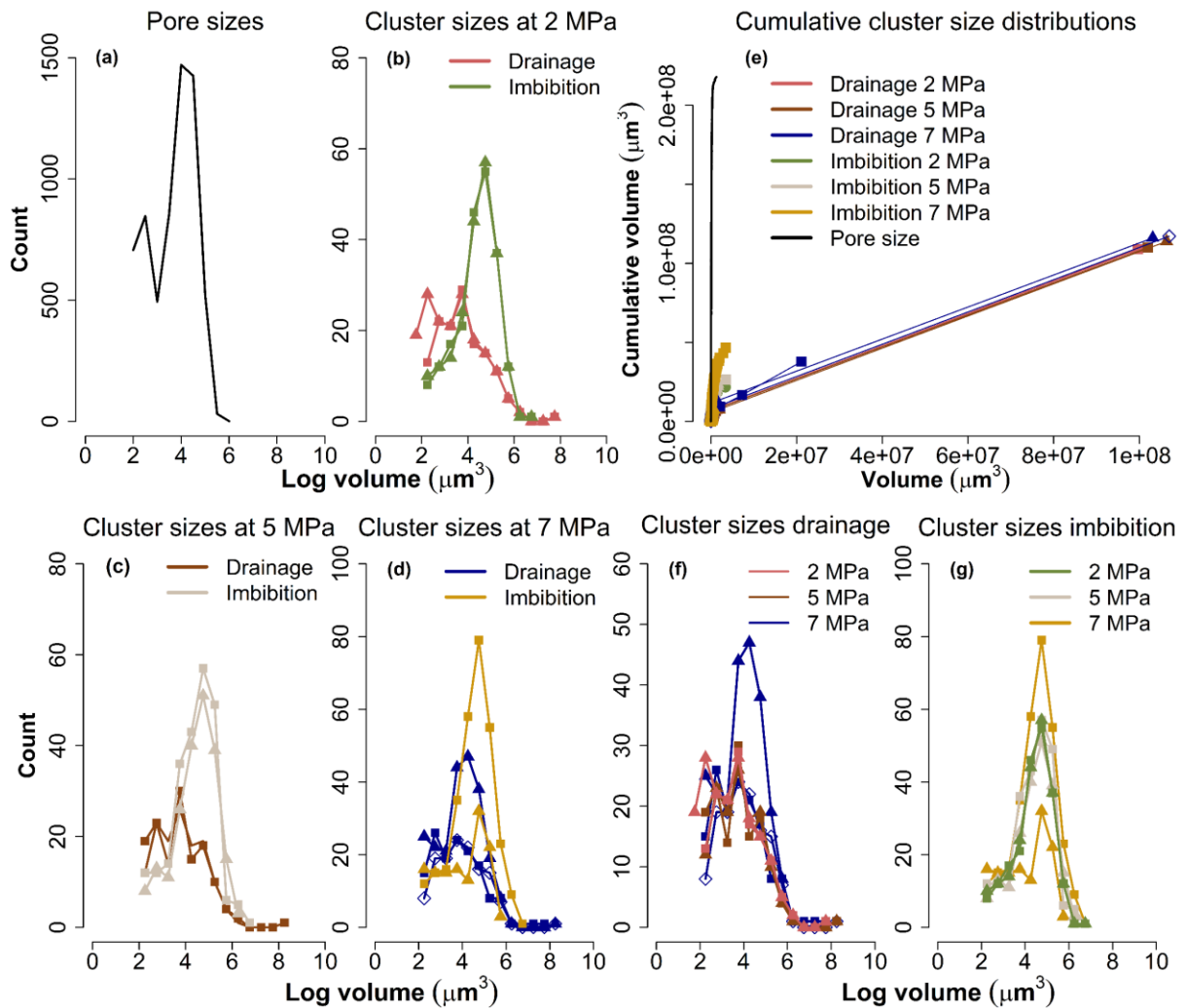
Fig. 5: **(a)** Pore size distribution as derived from the micro-CT image of the water-wet rock. Hydrogen cluster size distributions after drainage and imbition in experiments at 20 µl min⁻¹ flowrate and pore fluid pressures of 2 MPa **(b)**, 5 MPa **(c)** and 7 MPa **(d)**, and cumulative pore size and H_2 cluster size (CS) distributions at different pore fluid pressures **(e),** where squares, triangles and rhombi mark the distinct repeat experiments. **(f)** Hydrogen cluster size distribution after drainage for all experiments and **(g)** Hydrogen cluster size distribution after imbition for all experiments. Note the large H_2 clusters of ~10^8 μm^3 that exist after drainage in **(b)-(d)**. A decrease in the biggest cluster volume after imbition in **(b)-(d)** along with an increase in the number of small clusters marks the change in H_2 structure during the drainage and imbition processes. Histogram plots in **(a)-(d)**, **(f)** and **(g)** used a bin size of 10.

303

304   Hydrogen clusters during drainage were at all pore fluid pressures much larger than discrete

305   pores with a maximum volume of 1.3×10^6 µm^3 (Fig. 5e, a). Comparing all H$_2$ cluster size

306   distributions during drainage (Figure 5f) reveals that all drainage curves, including two of the

307   distributions at 7 MPa (squares and rhombi), have largely the same distribution, however one

308   of the three distributions at 7 MPa (triangles) is distinct. This outlier experiment corresponds

309   to the experiment showing a lower S_{nwi} (Fig. 4c).

310   Capillary trapping of H$_2$ during imbibition seemed independent of the pore fluid pressure with

311   10%, 12% and 4-21% of trapped H$_2$ at 2, 5 and 7 MPa, respectively (Fig. 4a-c,f, SI Fig. S3),

312   corresponding to 20%, 22% and 11-43% of the initially injected H$_2$. During imbibition, large

313   H$_2$ clusters were broken down into smaller clusters (Fig. 5a-d), in line with the visual changes

314   of the H$_2$ clusters (Fig. 4a-c and f). The largest H$_2$ clusters after imbibition remained above the

315   maximum pore size during all experiments except for one experiment at 7 MPa (triangles in

316   Fig. 5g, Fig. 5a), showing that not only was H$_2$ trapped in discrete pore bodies but also as larger

317   H$_2$ ganglia. The break-down of the largest H$_2$ clusters during imbibition caused the number of

318   clusters in the size range log 4 to log 6 µm^3 to increase while the number of very small clusters

319   of log 2-4 µm^3 typically decreased (Figs. 5b-d). Comparing all H$_2$ cluster size distributions

320   during imbibition (Figure 5g) shows that the distributions at 2 and 5 MPa are largely the same

321   while the imbibition distributions at 7 MPa are distinct.

322   Injections of H$_2$ and brine into the same rock volume and at the same flow rates and pore fluid

323   pressures of 2-5 MPa were repeatable with small standard errors between 0.01-0.66% (Fig. 4a

324   and b, Fig. 5b and c). At 7 MPa very distinct S_{nwi} and S_{nwr} were measured (Fig. 4c and f); During

325   drainage the standard error was 4.8% at an average H$_2$ saturation of 47.4%. The standard error

326   during imbibition was 8.5% at an average saturation of 12.9%. The pressure differences

327   between inlet and outlet during these experiments were within the error of the pressure sensors

328   of 0.1% full-scale.

329   *3.3 Effect of hydrogen/brine injection ratio on*

330   *hydrogen connectivity and saturation*

331   We studied the effect of the H_2/brine injection

332   ratio on the H_2 saturation in order to evaluate

333   the effect of H_2 injection into hydrodynamic

334   aquifers, and to evaluate what happens in the

335   far field, where fluids will be moving together.

336   The results showed that the H_2 saturation and

337   H_2 interconnected pore volume increased with

338   increasing H_2/brine injection ratio from 32.6%

339   at 4 µl min^{-1} H_2 plus 16 µl min^{-1} brine to 43.2%

340   at 16 µl min^{-1} H_2 plus 4 µl min^{-1} brine (Fig. 6).

341   The H_2 clusters in simultaneous injection

342   experiments occupied many of the same pore

343   spaces as the clusters after H_2 in the non-

344   steady state experiments at the same pressure

345   and total flowrate (Fig. 4b, Fig. 6, SI Fig. S5),

346   and even at the lowest H_2 brine injection ratio

347   of 4 µl min^{-1} H_2 plus 16 µl min^{-1} brine, the H_2

348   clusters were large, and spanning multiple

349   pores. The percolation threshold, i.e. one

350   connected path from inlet to outlet, was

351   apparently only reached at 100% H_2 injection

352   (Fig. 4b vs. Fig. 6, SI Fig. S5). The pressure

(a) 1:4 H_2/ brine

32.6 %

(b) 1:1 H_2/ brine

34.6 %

(c) 4:1 H_2/ brine

1 mm   43.2 %
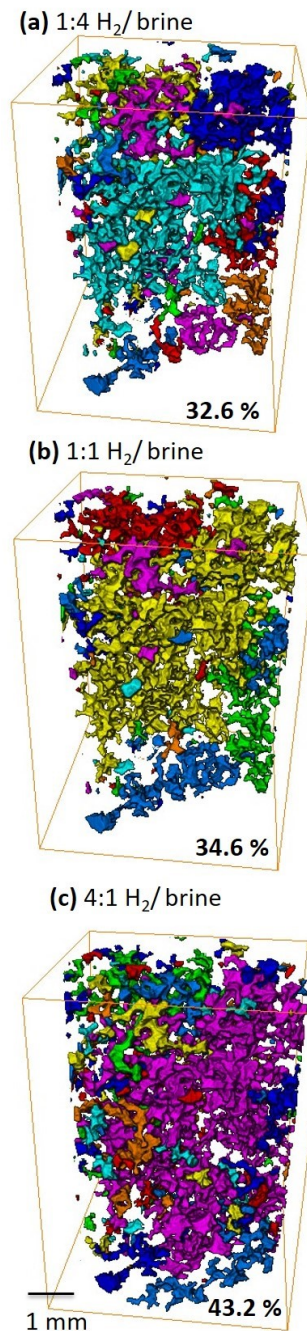
Fig. 6: Effect of H_2/brine injection ratio on H_2 saturation and H_2 connectivity during simultaneous H_2 and brine injection at 5 MPa **(a)** 4 µl min^{-1} H_2 plus 16 µl min^{-1} brine, **(b)** 10 µl min^{-1} H_2 plus 10 µl min^{-1} brine, **(c)** 16 µl min^{-1} H_2 plus 4 µl min^{-1} brine. Discrete H_2 clusters were rendered in colours, where mainly one color marks one large, connected cluster and different colors indicate several, not connected clusters. With increasing injection ratio H_2 saturation and H_2 connectivity increase.

353 differences between inlet and outlet

354 during the simultaneous injection

355 experiments were up to 0.05 MPa.

356 The H$_2$ cluster volume distributions

357 were similar at different H$_2$:brine

358 injection ratios (Fig. 7a). However, with

359 increasing ratio the smallest H$_2$ clusters

360 of volume ~log 2 μm^3 decreased in

361 number while the number of

362 intermediate size (log 2.5 to log 6.25

363 μm^3) H$_2$ clusters and the volume of the

364 biggest cluster increased (Fig. 7a),

365 confirming observations of increasing

366 H$_2$ saturation and connectivity with

367 increasing injection ratio (Fig. 6).
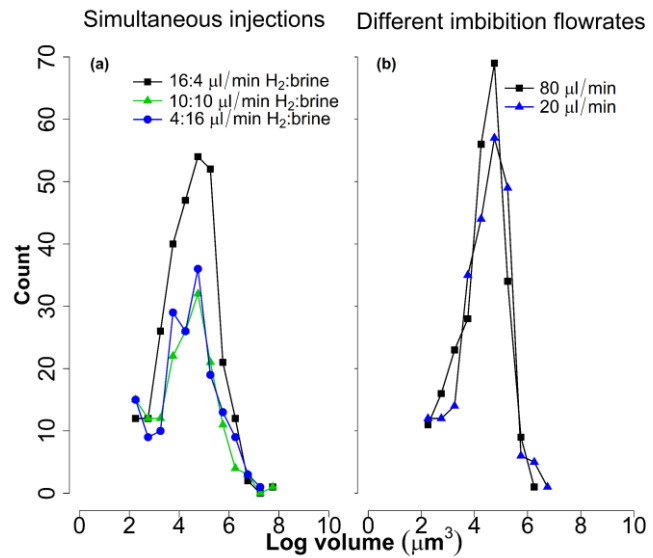
Fig. 7. **(a)** H$_2$ cluster size distributions during simultaneous injections of H$_2$ and brine at flowrate ratios of 16:4, 10:10 and 4:16 µl min^{-1} H$_2$:brine and 5 MPa injection pressure. As the flowrate ratio of H$_2$ to brine increased, the number of intermediate size H$_2$ clusters increased and the radius of the biggest cluster increased. **(b)** Effect of flowrate during brine imbibition. All plots used a bin size of 10.

368 *3.4 Effect of flowrate on hydrogen saturation and recovery*

369 At constant pore fluid pressure of 5 MPa, increases in the flowrate during drainage from 20 µl

370 min^{-1} to 80 µl min^{-1}, corresponding to bulk N_C of 1.7 x10^{-8} to 6.8x10^{-8}, respectively, decreased

371 the H$_2$ saturation from to 51.7% to 47.7% (Figure 4b and d). Correspondingly, increases in the

372 brine flowrate during imbibition from 20 µl min^{-1} to 80 µl min^{-1}, corresponding to bulk N_C of

373 2.4x10^{-6} and 9.4x10^{-6}, respectively, reduced the S$_{nwr}$ from 11.5% to 7.2% (Fig. 4b and d).

374 In line with this, the H$_2$ cluster size distributions at the two flowrates showed that larger clusters

375 were mobilized at 80 µl min^{-1} (maximum cluster sizes of log 6.25 μm^3 at 80 µl min^{-1} vs. log

376 6.75 μm^3 at 20 µl min^{-1}; Fig. 7b). At both flowrates the largest H$_2$ clusters were still bigger than

377   the largest pore of <log 6 μm^3 (Fig. 7b vs. Fig 6a), indicating that H_2 was trapped also as larger

378   ganglia.

379   *3.5 Secondary drainage and imbibition*

380   Secondary drainage and imbibition did not significantly change the H_2 saturation (47.9% and

381   7.0%) compared to primary drainage and imbibition (47.6% and 7.3%), based on results at 5

382   MPa and 80 $\mu l \ min^{-1}$ flowrate (SI Fig. S4, Fig. 4d-e).

383   *3.6 Dry rock experiment*

384   In the dry-rock experiment, the brine entered the H_2-filled dry rock via piston-like

385   displacement, (Fig. 8b), eventually recovering the H_2 entirely (Fig. 8d). Before all H_2 was

386   recovered, there was an intermediate stage where previously brine-filled pores (Fig. 8b)

387   showed several very small H_2 bubbles (Fig. 8d).

388   *3.7 Comparison to nitrogen*

389   The N_2 saturation was similar to the H_2 saturation during drainage (48.7% vs. 51.7 ± 0.66%,

390   respectively) but N_2 saturation after brine imbibition was much higher (33.9% vs. 11.5 ±

391   0.64%, respectively; Fig. 4e, SI Fig. S6). The N_c of H_2 and N_2 during drainage were 1.7×10^{-8}

392   and 3.5×10^{-8}, respectively.

393

394   **4. Discussion**

395   *4.1 Pore space*

396   The μCT-evaluated porosity of the Clashach sandstone from the segmented volume of the

397   water-saturated rock of 12.5-13.6% was within the range of the published porosities of 11.1-

398   14.4% for Clashach sandstone[42-44]. The distributions of pore size and pore throat size as

399   evaluated by μCT and MICP, respectively, suggested that mostly small pores of <50 μm radii

400   were joined by very small throats of <5 μm radii with a few small to intermediate size throats
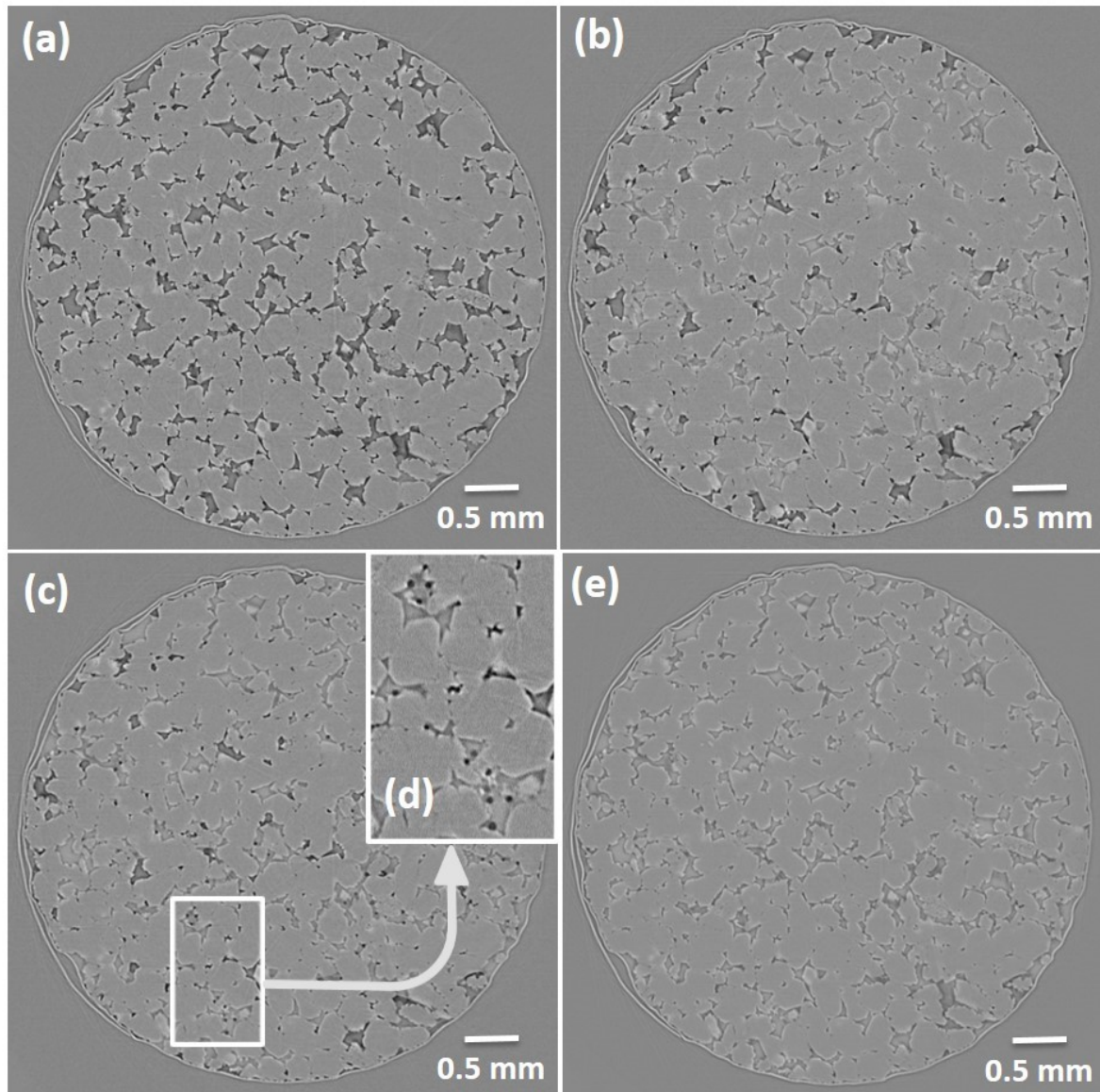
Fig. 8. The dry-rock experiment summarized. **(a)** H_2-saturated, dry rock, **(b)** scan during brine imbibition shortly after appearance of the first brine in the rock, **(c)** scan during brine imbibition after 115 minutes, with several small, isolated H_2 bubbles inside pore bodies **(d),** and **(e)** brine-saturated rock after two hours of imbibition showing 100% recoverability of H_2.

of >5 to 90 μm radii in between (Fig. 2). The largest pore throat of 195 μm radius was probably measured at the surface of the rock core where the drilling process affected the pore space. The pore throat distribution for our Clashach sandstone sample was very similar to the pore throat distribution for Berea sandstone[54]. Compared to the pore throat distributions for Bentheimer

411 sandstone and Doddington sandstone[54], our Clashach sandstone sample showed smaller pore

412 throat sizes. Limestones generally show a wider pore throat size distributions than sandstones[54].

413 *4.2 H₂ flow behaviour and trapping mechanisms*

414 Hydrogen behaved as a non-wetting phase, filling the centre of the pores, with residual brine

415 in the pore corners and throats (Fig. 3b and c), indicating a water wetting system. The largest

416 H_2 cluster was much larger than discrete pores at any pore fluid pressure during drainage (Fig.

417 5), indicating a good connectivity of the H_2[55]. Hydrogen trapping occurred via snap-off of H_2

418 ganglia (Fig. 9). Snap-off competes with piston-like, i.e. pore-filling, displacement during the

419 displacement of a non-wetting fluid by a wetting fluid in porous media[21], and is known as the

420 swelling of water in the corner layers of a pore throat during water invasion in water-wet porous

421 rocks until the threshold capillary pressure is exceeded, resulting in spontaneous filling of the

422 throat with water and disconnection of the non-wetting phase which can lead to trapping[21].

423 Brine films around grains were not directly visible in the tomographic images (Fig. 3b and c)

424
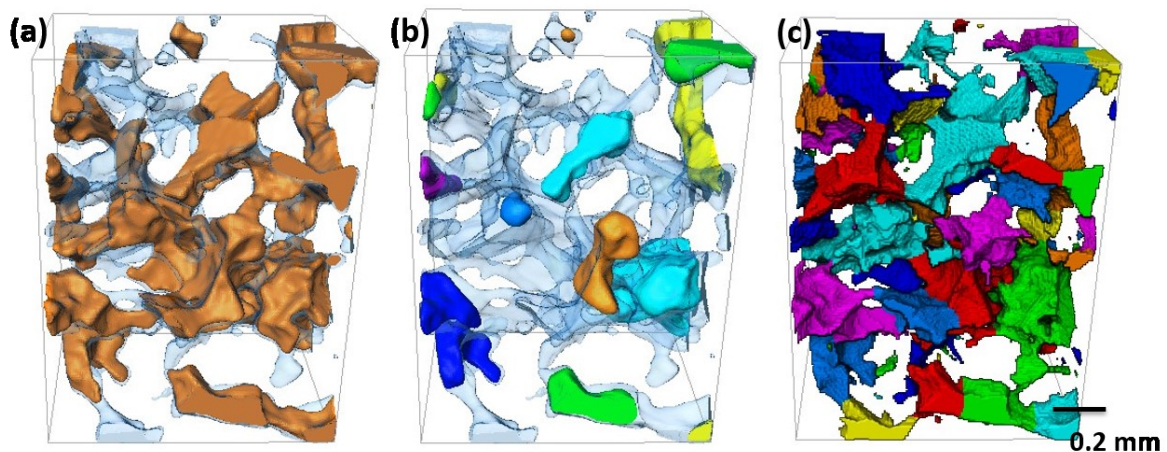
Fig. 9: Example of a snap-off event. **(a)** Labelled H_2-filled volume after drainage (orange), spanning over several pores, and total pore space (transparent blue) showing one large interconnected H_2-filled pore volume. **(b)** Labelled H_2-filled volume after brine imbibition (different coloured shades) and the total pore space (transparent blue) showing several, not connected H_2 ganglia and the snapped-off H_2 droplet (cobalt blue) in the centre, left hand side. **(c)** Pore body visualisation of the same volume.

425 but were revealed by subtraction of the water-saturated scan from the brine-saturated scan after

426 H_2 injection, following the registration of the brine-saturated scan after H_2 injection to the

427 water-wet scan (Fig. 3d and e). Figures 3d and 3e suggest that brine films were discontinuous

428 and very thin. When H_2 was injected into a dry rock, 100% of the injected H_2 could be recovered

429 (Fig. 8e) which substantiated the theory that sub-resolution brine films around grains and snap-

430 off of H_2 ganglia caused decreased H_2 recovery in experiments using an initially brine saturated

431 rock (UoE experiments). The occurrence of several very small H_2 bubbles in the dry-rock

432 experiment (Fig. 8d) indicated Roof snap-off[56] of H_2 ganglia.

433 *4.3 Effect of pore fluid pressure and hydrogen/brine injection ratio*

434 We observed no dependence of the H_2 saturation during drainage on pore fluid pressure,

435 considering that 2 out of 3 experiments at 7 MPa showed the same the same H_2 saturation of

436 ~50 % as at 2 and 5 MPa (Fig. 4a-c,f, and SI Fig. S3). The one experiment at 7 MPa which had

437 only 39.7% H_2 saturation (Fig. 4c, SI Fig. S3 and blue triangles in Fig. 5f) did also not have

438 the same H_2 cluster size distribution as the remaining experiments (Fig. 5f), despite using the

439 same experimental settings as for all other experiments at 7 MPa, and the log archives of the

440 pore fluid pressures and injected volumes revealed no abnormalities. A shift in the distribution

441 of cluster sizes can indicate a change in wettability, regardless of the measured H_2 saturation.

442 Yet, as two of the results at 7 MPa showed a similar distribution as at the other pressures, it

443 seems likely that this experiment is an outlier. The experiment was acquired after a filament

444 change on the μCT apparatus, which implied that a slightly different part of the same rock core

445 was imaged (13.6% vs. 12.5% porosity). Yet, in principle this should not have affected the

446 results significantly, and subsequent experiments did return to show ~50% H_2 saturation, e.g.

447 the H_2 stability experiment (SI Fig. S2).

448 The observed constant drainage H_2 saturations with increasing pore fluid pressures from 2 to 7

449 MPa are in line with a lack of a dependence of the H_2 wettability on pressure increases from 2-

450   10 MPa in Berea and Bentheimer sandstone[18], with only very small increases of ~3-6° in the

451   H_2 contact angles at pressure increases from 2 to 7 MPa in Basalt[21] and clay[24] and quartz[19], and

452   with a previous findings of no change in the characteristic trapping curves for CO_2 and N_2 at a

453   wide range of pressure and temperature conditions[35]. The general anticipation of an increase in

454   gas saturation with injection pressure[57, 58] may still be valid over pressure ranges larger than

455   the one investigated here. At unchanged wettability, the S_{nwi} is controlled by the capillary

456   pressure which in turn is controlled either by the fractional flow (during simultaneous injection)

457   or by the viscous force pressure drop (during single fluid phase injection). Thus, the

458   independence of the S_{nwi} from the pore fluid pressure indicates that the viscous pressure drop

459   is not being significantly altered by the changing pressure, e.g., the H_2 viscosity change is not

460   having a major impact on the force required to drive flow. Significant loss of H_2 from the gas

461   phase at higher pressures by dissolution into the brine is precluded by the low solubility of H_2

462   of ~0.02 mol kgw^{-1} at 2.5 MPa[59]. The H_2 stability experiments showed that H_2 saturation at 5

463   MPa did not change over a time period of ten hours (49.55% at time zero vs. 49.53% ten hours

464   after; SI Fig. S2), evidencing a stable result and no H_2 loss by dissolution.

465   Looking at the S_{nwr} data only (Fig. 4a-c,f), there was no clear dependency on pore fluid pressure

466   during imbibition. Any change may, however, have been masked by the high variation between

467   the two results at 7 MPa (4-21% Fig. 4c and f). Considering that the experiment at 7 MPa with

468   the low S_{nwi} of 40% could be identified as an outlier (see the discussion in the beginning of

469   section 4.3, and Fig. 5f, blue triangles) and that the S_{nwr} is a function of the S_{nwi} where a lower

470   S_{nwi} will tend to overestimate recovery[54, 60], we may disregard the S_{nwr} of 4%. The large increase

471   in trapped H_2 in the second full primary drainage and secondary imbibition experiment at 7

472   MPa (Fig. 4f) was probably due to the poorer intial H_2 connectivity[60]. The H_2 cluster size

473   distribution for this experiment showed an increase in the number of intermediate size clusters

474   compared to the other experiments (Fig. 5g, darkyellow squares), without however shifting the

475 cluster distribution, suggesting no wettability change. This indicates that variation in one or

476 more of the other thermophysical properties –density, viscosity, or IFT – have resulted in the

477 impact on the pore scale fluid configuration (Figure 10). Meanwhile, a poorer initial H_2

478 connectivity was not confirmed by the third repetition of primary drainage at 7 MPa (SI Fig.

479 S3g). More experiments at 7 MPa are needed to confirm the result of increased trapping at

480 higher pore fluid pressures.

481
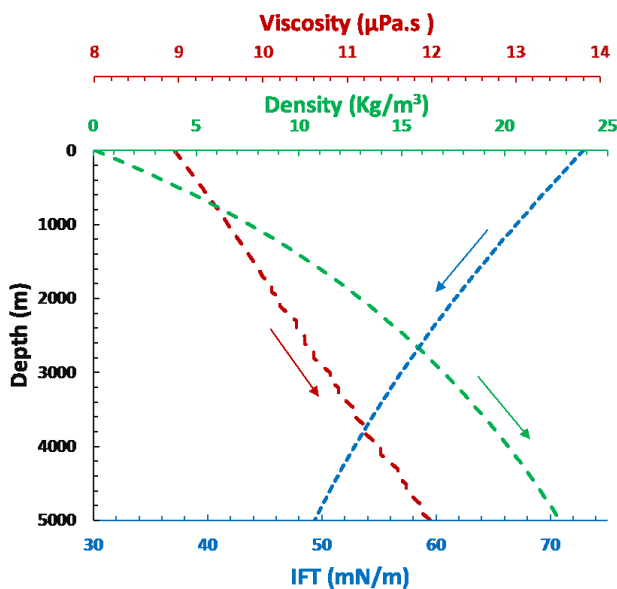
Fig. 10: Density (green line), viscosity (red line), and interfacial tension (blue line) of hydrogen versus depth (Hassanpouryouzband et al. 2021)[61].

482

483 Given a hydrostatic gradient of ~10 MPa/km an increase of the S_{nwr} with increasing pore fluid

484 pressure, as suggested by the second experiment at 7 MPa (Fig. 4f), would indicate that deeper

485 aquifers are less favourable for H_2 storage operations. However, unlike our non-steady state

486 experiments which showed barely any pressure difference between inlet and outlet, in a real

487 H_2 storage operation, the well pressure is significantly higher than the reservoir pressure and

488 the brine is not injected, but naturally flowing into previously H_2-saturated rock when the H_2

489   is recovered- again due to a pressure difference. Our displacement study results are hence

490   applicable to the fringe of the H_2-saturated zone, only, where pressure differences are very

491   small. A decreased H_2 recovery with depth would not align well with other criteria for an

492   economical and safe H_2 storage operation, such as a lower cushion gas requirement with

493   elevated depth[5] and reduced risks for H_2-linked microbial activity at higher depths due to higher

494   temperatures[6].

495   The pressure/depth effect on our results can be further related to the variation of key pore-scale

496   displacement parameters for H_2 with depth (Fig. 10): The IFT of H_2 reduces with depth whereas

497   the H_2 viscosity increases, both of which in theory should augment the displacement of H_2 with

498   water and reduce the S_{nwr}[62, 63]. However, increased S_{nwr} with decreasing IFT and increasing

499   viscosity has also been demonstrated[64] which may be due to a simultaneously increased

500   likelihood of unstable displacement/ non-uniform fronts[10, 65] during both drainage and

501   imbibition processes at decreasing IFT and increasing viscosity, based on the augmenting effect

502   of both parameters on N_C (Eq. 1). Such unstable displacement processes at higher pore fluid

503   pressures, addition to a variation in the thickness of the brine thin films with pressure, may

504   explain the decrease in interconnected H_2-filled pore volume from one large cluster at 2-5 MPa

505   to three clusters at 7 MPa and have lead to increased snap-off and trapping during imbibition

506   (Fig. 4f).

507   The S_{nwr} of 10-21% was significantly less than the previously reported H_2 S_{nwr} of 41% for a

508   sandstone under ambient conditions[40]. As mentioned previously, the short length rock sample

509   in Jha et al. (2021)[40] suggests that their results were affected by capillary end effects[46].

510   However, the applied the relatively high bulk brine N_C of 2.4×10^{-6} may have mobilised more

511   residual H_2 than under strict capillary regime conditions.

512   During simultaneous injection of H_2 and brine, which may be representative of H_2 injection

513   into hydrodynamic aquifers or simulate the far field conditions, H_2 saturation and H_2

514   interconnected pore volume increased with increasing H_2/brine injection ratio (Fig. 6). This

515   indicated that a lower brine flow is favoured over high flow environments in terms of

516   optimising the H_2 storage operation. The structure was apparently not percolating in any of the

517   simultaneous injection experiments as opposed to during 100% H_2 injection (Fig. 6 vs. Fig.

518   4b), yet considering significant pressure differences of up to 0.05 MPa between inlet and outlet

519   in simultaneous injection experiments which were not observed in experiments injecting 100%

520   H_2, the connections between the H_2 clusters may have been broken when the injection (and

521   thereby the pressure gradient) was stopped for the scan.

522   *4.4 Effect of capillary number on initial and residual saturation*

523   Classical pore-scale displacement theory predicts little change in residual phase saturation in

524   response to increases in flow rate until N_C exceeds 10^{-6} -10^{-5}. However, for most subsurface

525   reservoirs there will be rapid decreases at N_C of 10^{-4} or more, when viscous forces become

526   dominant[54]. The bulk brine N_C applied in this study (2.4-9.4x10^{-6}) was within the range of little

527   saturation change but exceeded the threshold of N_C <10^{-6} for which the flow generally is said

528   to be capillary dominated[54]. This may indicate that viscous forces caused a significant effect of

529   N_C on the S_{nwr} in our experiments (Fig. 4b and d), and these forces are likely to be even greater

530   at local scale than at bulk[54]. The H_2 cluster size distribution after imbibition at N_C= 9.4x10^{-6}

531   was shifted with respect to the distribution at N_C= 2.4x10^{-6} (Fig. 7b), indicating a change in the

532   wetting behaviour and supporting previous findings of preferential desaturation of larger

533   clusters at higher Nc[66].

534   We observed a 4% decrease in S_{nwi} in our experiments when bulk N_C was increased from

535   1.7x10^{-8} to 6.8x10^{-8} (Fig. 4b and d). Critical nonwetting phase N_C of 2x10^{-8} and 10^{-5} during

536   imbibition have been reported for water–gas systems and water-oil systems, respectively[67],

537   indicating that the threshold of N_C <10^{-6} for capillary dominated flow[54] is not rigid. However,

538   considering reported increases in the H_2 saturation after drainage with increasing N_C from

539   7.7×10^{-7} to 7.7×10^{-5} [20], and acknowledging the small observed difference in S_{nwi}, we cannot

540   exclude that the effect of flow rate was down to experimental variability.

541   *4.5 Comparison to nitrogen*

542   The N_2 saturation was comparable to the H_2 saturation during drainage at similar N_C of $1\text{-}3 \times 10^{-}$

543   ^{8} but the S_{nwr} after imbibition was ~20 % higher for N_2 than for H_2 (Fig. 4b and e). Using N_2 as

544   a proxy for H_2 in experimental drainage and imbibition studies is hence not advisable.

545   Considering the high degree of N_2 trapping, the use of N_2 as a cushion gas for H_2 storage

546   operations which could reduce operational costs[8] seems favourable. Our results are lower than

547   a reported 64% intial N_2 saturation during drainage and 43% residual N_2 saturation during brine

548   (200 g/L NaI +15 g/L $CaCl_2$) imbibition in a Berea sandstone (20-22% porosity) at 5.5 MPa

549   and 20°C[37], and higher than 43% N_2 saturation during drainage in a Bashijiqike tight sandstone

550   (5.6% porosity) at 8 MPa and ambient temperature[36]. The trend in the differences of the N_2

551   saturation in the above studies follows the same trend as the differences in the porosities of the

552   studied sandstones, with the Clashach sandstone (14% porosity) being intermediate between

553   the two other rocks. This indicates that porosity differences between the different rock types

554   applied in the above experiments defined the observed N_2 saturations, yet differences in the

555   pore throats dimensions may equally have contributed or caused this. Hence S_{nwi} and S_{nwr}

556   depend strongly on (the local conditions within) each rock, and these rock type/local effects

557   may mask any effect of injection conditions. However, trends in the rock-specific behaviour

558   will be controlled by pressure and flow conditions. It follows from this that any rock selected

559   for H_2 storage operations has to be very well characterized, in particular with respect to

560   porosity, turtoisity and capillary pressure curves.

561   *4.6 Suitability of the Clashach sandstone for hydrogen storage*

562   It has been postulated that the low viscosity of H_2 will cause the gas to travel swiftly, making

563   it little suitable for displacing brine[10] and causing low H_2 injectivity. In this work, we showed

564   that from an injectivity and recovery perspective, untreated Clashach sandstone is suitable for

565   underground H_2 storage. However, sandstones aged by exposure to humic acids may be more

566   suitable analogue rocks for experimental investigations of H_2 storage in porous media[19].

567   Considering that aging has previously been shown to alter the wettability of H_2 brine-quartz

568   systems from highly water-wet toward intermediate-wet[19] the stated H_2 saturations for our

569   untreated outcrop Clashach sandstone are expected to increase during drainage and decrease

570   during imbibition, further the increasing suitability for H_2 storage.

571

572   **5. Conclusion**

573   In this work, a prima facie examination of H_2 flow and displacement processes in porous rock

574   was carried out as a function of capillary numbers of $1.2\text{-}6.8\times10^{-8}$ for H_2 and $2.4\text{-}9.5\times10^{-6}$ for

575   brine, and of pore fluid pressures between 2-7 MPa. Results showed no clear relation between

576   pore fluid pressure and H_2 saturation with ~50% of the pore space saturated with H_2 during

577   drainage at all pressures, and 20%, 24% and 43% of the initial H_2 trapped at 2, 5 and 7 MPa,

578   respectively, during imbibition at a capillary number of 2.4×10^{-6}, indicating that higher

579   pressure, i.e. deeper reservoirs are less favourable for H_2 storage. Injection of brine at higher

580   capillary numbers reduced capillary trapping and increased H_2 recovery. Hydrogen recovery

581   was distinct from N_2 recovery, suggesting that N_2 is a poor proxy for H_2. Based on these results,

582   we recommend more shallow, lower pressure sites for future H_2 storage operations in porous

583   media. Future work should aim to measure the influence of pressures above 7 MPa, elevated

584   temperatures and rock aging on H_2 and brine displacement processes at a range of different

585   capillary numbers. Dynamic experiments using synchrotron light sources are recommended to

586   examine displacement mechanisms closely.

587

Author Contributions

589 The experimental kit was built by Butler and Thaysen. Experiments were carried out by Thaysen,
590 Butler, Hassanpouryouzband, Freitas. Alvarez-Borges, Atwood and Humphreys were the
591 supporting beamline scientists during the experiments at Diamond Light Source. Image
592 reconstruction and tomographic analysis was carried out by Thaysen. Interpretation of the results
593 was by Thaysen, Butler, Hassanpouryouzband, Krevor and Heinemann. The manuscript was
594 written by Thaysen with review by Butler, Krevor Heinemann, Hassanpouryouzband, Freitas and
595 Edlmann. All authors have given approval to the final version of the manuscript.

596

Declaration of interest

598 The authors declare no competing interest.

599

Funding Sources

References

1.   Tarkowski, R., Underground hydrogen storage: Characteristics and prospects *Renew Sust Energ Rev* **2020,** *105*, 86-94.

2.   Beckingham, L. E.; Winningham, L., Critical knowledge gaps for understanding water-rock-working phase interactions for compressed energy storage in porous formations. *Acs Sustain Chem Eng* **2020,** *8* (1), 2-11.

3.   Mouli-Castillo, J.; Heinemann, N.; Edlmann, K., Mapping geological hydrogen storage capacity and regional heating demands: An applied UK case study. *Appl Energy* **2021,** *283* (116348).

4.   Hassanpouryouzband, A.; Joonaki, E.; Edlmann, K.; Heinemann, N.; Yang, J., Thermodynamic and transport properties of hydrogen containing streams. *Sci Data* **2020,** *1* (1), 1-14.

5.   Heinemann, N.; Booth, M. G.; Haszeldine, R. S.; Wilkinson, M.; Scafidi, J.; Edlmann, K., Hydrogen storage in porous geological formations - onshore play opportunities in the Midland Valley (Scotland, UK). *Int J Hydrog Energy* **2018,** *43* (45), 20861-20874.

6.   Thaysen, E. M.; McMahon, S.; Strobel, G. J.; Butler, I. B.; Ngwenya, B. T.; Heinemann, N.; Wilkinson, M.; Hassanpouryouzband, A.; McDermott, C. I.; Edlmann, K., Estimating microbial growth and hydrogen consumption in hydrogen storage in porous media *Renew Sustain Energ Rev* **2021,** *151* (111481), 1-15.

7.   Matos, C. R.; Carneiro, J. F.; Silva, P. P., Overview of large-scale underground energy storage technologies for integration of renewable energies and criteria for reservoir identification. *J. Energy Storage* **2019,** *21*, 241-258.

8.   Heinemann, N.; Alcalde, J.; Miocic, J.; Hangz, S. J. T.; Kallmeyer, J.; Ostertag-Henning; Hassanpouryouzband, A.; Thaysen, E. M.; Strobel, G.; Wilkinson, M.; Schmidt-Hattenberger, C.; Edlmann, K.; Bentham, M.; Haszeldine, S.; Carbonell, R.; Rudloff, A.,

638   Enabling large-scale hydrogen storage in porous media: the scinetific challenges. *Energy*

639   *Environ Sci* **2021,** *14*, 853-864.

640   9.   Paterson, L., The implications of fingering in underground hydrogen storage. *Int J*

641   *Hydrogen Energ* **1983,** *8* (1), 53-59.

642   10.   Chaturvedi, K. R.; Bajpai, S.; Trivedi, J.; Sharma, T., Air foams for mobility control

643   and subsurface storage of hydrogen in porous media: An experimental study. *Energy & Fuels*

644   **2022,** *36*, 5036-5046.

645   11.   Flesch, S.; Pudlo, D.; Albrecht, D.; Jacob, A.; Enzmann, F., Hydrogen underground

646   storage-Petrographic and petrophysical variations in reservoir sandstones from laboratory

647   experiments under simulated reservoir conditions. *Int J Hydrog Energy* **2018,** *43* (45), 20822-

648   20835.

649   12.   Yekta, A. E.; Pichavant, M.; Audigane, P., Evaluation of geochemical reactivity of

650   hydrogen in sandstone: Application to geological storage. *J Appl Geochem* **2018,** *95*, 182-

651   194.

652   13.   Hassanpouryouzband, A.; Adie, K.; Cowen, T.; Thaysen, E. M.; Heinemann, N.;

653   Butler, I. B.; Wilkinson, M.; Edlmann, K., Geological Hydrogen Storage: Geochemical

654   Reactivity of Hydrogen with Sandstone Reservoirs. *ACS Energy Lett* **2022,** *7*, 2203-2210.

655   14.   Yekta, A. E.; Manceau, J. C.; Gaboreau, S.; Pichavant, M.; Audigane, P.,

656   Determination of Hydrogen-Water Relative Permeability and Capillary Pressure in

657   Sandstone: Application to Underground Hydrogen Injection in Sedimentary Formations.

658   *Transport Porous Med* **2018,** *122* (2), 333-356.

659   15.   Rezaei, A.; Hassanpouryouzband, A.; Molnar, I.; Derikvand, Z.; Haszeldine, R. S.;

660   Edlmann, K., Relative permeability of hydrogen and aqueous brines in sandstones and

661   carbonates at reservoir conditions. *Geophys Res Lett* **2022**.

662   16.   Higgs, S.; Da Wang, Y.; Sun, C.; Ennis-King, J.; Jackson, S. J.; Armstrong, R. T.;

663   Mostaghimi, P., In-situ hydrogen wettability characterisation for underground hydrogen

664   storage. *Int J Hydrog Energy* **2021,** *47* (26), 13062-13075.

665   17.   Esfandyari, H.; Sarmadivaleh, M.; Esmaeilzadeh, F.; Ali, M.; Iglauer, S.;

666   Keshavarz, A., Experimental evaluation of rock mineralogy on hydrogen-wettability:

667   Implications for hydrogen geo-storage. *J Energy Storage* **2022,** *52* (104866), 1-8.

668   18.   Hashemi, L.; Glerum, W.; Farajzadeh, R.; Hajibeygi, H., Contact angle measurement

669   for hydrogen/brine/sandstone system using captive-bubble method relevant for underground

670   hydrogen storage. *Adv Water Resour* **2021,** *154* (103964), 1-13.

671   19.   Iglauer, S.; Muhammad, A.; Keshavarz, A., Hydrogen wettability of sandstone

672   reservoirs: implications for hydrogen geo-storage. *Geophys Res Lett* **2020,** *48* (3), 1-5.

673   20.   Lysyy, M.; Ersland, G.; Fernø, M., Pore-scale dynamics for underground porous

674   media hydrogen storage. *Adv Water Resour* **2022,** *163* (104167), 1-13.

675   21.   Al-Yaseri, A.; Jha, N. K., On hydrogen wettability of basaltic rock. *J Pet Sci Eng*

676   **2021,** *200*, 1-5.

677   22.   Hosseini, M.; Ali, M.; Fahimpour, J.; Keshavarz, A.; Iglauer, S., Basalt-H_2-brine

678   wettability at geo-storage conditions: Implication for hydrogen storage in basaltic formation.

679   *J Energy Storage* **2022,** *52* (104745), 1-6.

680   23.   van Rooijen, W.; Hashemi, L.; Boon, M.; Farajzadeh, R.; Hajibeygi, H.,

681   Microfluidics-based analysis of dynamic contact angles relevant for underground hydrogen

682   storage. *Adv Water Resour* **2022,** *164* (104221), 1-17.

683   24.   Al-Yaseri, A.; D., W.-B.; Fauziah, C. A.; Iglauer, S., Hydrogen wettability of clays:

684   Implications for underground hydrogen storage. *Int J Hydrog Energy* **2021,** *46* (69), 34356-

685   34361.

686   25.   Azin, R.; Izadpanahi, A., *Fundamentals and practical aspects of gas injection*

687   Springer: 2022.

688   26.   Morrow, N.; Chatzis, I.; Taber, J. J., Entrapment and mobilization of residual oil in

689   bead packs. *SPE Reservoir Engineering* **1988,** *3* (3).

690   27.   Blunt, M. J.; Bijeljic, B.; Dong, H.; Gharbi, O.; Iglauer, S.; Mostaghimi, P.;

691   Paluszny, A.; Pentland, C. H., Pore-scale imaging and modelling. *Adv Water Resour* **2013,**

692   *51*, 197-216.

693   28.   Saraf, S.; Bera, A., A review on pore-scale modeling and CT scan technique to

694   characterize the trapped carbon dioxide in impermeable reservoir rocks during sequestration.

695   *Renew Sust Energ Rev* **2021,** *144* (110986), 1-20.

696   29.   Xu, L.; Myers, M.; Li, Q.; White, C.; Zhang, X., Migration and storage

697   characteristics of supercritical CO_2 in anisotropic sandstones with clay interlayers based on

698   micro-CT experiments. *J Hydrol* **2020,** *580* (124239), 1-17.

699   30.   Iglauer, S.; Paluszny, A.; Pentland, C. H.; Blunt, M. J., Residual CO_2 imaged with x-

700   ray micro-tomography. *Geophys Res Lett* **2011,** *38* (L21403), 1-6.

701   31.   Andrew, M.; Menke, H.; Blunt, M. J.; Bijeljic, B., The imaging of dynamic

702   multiphase fluid flow using synchrotron-based x-ray microtomography at reservoir

703   conditions. *Tranp Porous Med* **2015,** *110* (1), 1-24.

704   32.   Andrew, M.; Bijeljic, B.; Blunt, M. J., Pore-scale imaging of trapped supercritical

705   carbon dioxide in sandstones and carbonates. *Int J Greenh Gas Control* **2014,** *22*, 1-14.

706   33.   Krevor, S. C. M.; Pini, R.; Zuo, L.; Benson, S. M., Relative permeability and

707   trapping of CO_2 and water in sandstone rocks at reservoir conditions. *Water Resour Res* **2012,**

708   *48*, 1-16.

709   34.   Rahman, T.; Lebedev, M.; Barifcani, A.; Iglauer, S., Residual trapping of

710   supercritical CO_2 in oil-wet sandstone. *J Colloid Interf Sci* **2016,** *469*, 63-68.

711   35.   Niu, B.; Al-Menhali, A.; Krevor, S. C., The impact of reservoir conditions on the

712   residual trapping of carbon dioxide in Berea sandstone. *Water Resour Res* **2015,** *51* (4), 2009-

713   2029.

714   36.   Cao, Q.; Gong, Y.; Fan, T.; Wu, J., Pore-scale simulations of gas storage in tight

715   sandstone reservoirs for a sequence of increasing injection pressure based on micro-CT. *J Nat*

716   *Gas Sci Eng* **2019,** *64*, 15-27.

717   37.   Khishvand, M.; Alizadeh, A. H.; Piri, M., In-situ characterization of wettability and

718   pore-scale displacements during two- and three-phase flow in natural porous media. *Adv*

719   *Water Resour* **2016,** *97*, 270-298.

720   38.   Sarmadivaleh, M.; Al-Yaseri, A.; Iglauer, S., Influence of temperature and pressure

721   on quartz–water–CO_2 contact angle and CO_2–water interfacial tension. *J Colloid Interf Sci*

722   **2015,** *441*, 59-64.

723   39.   Al-Yaseri, A.; Esteban, L.; Giwelli, A.; Sarout, J.; Lebedev, M.; Sarmadivaleh, M.,

724   Initial and residual trapping of hydrogen and nitrogen in Fontainebleau sandstone using

725   nuclear magnetic resonance core flooding. *Int J Hydrog Energy* **2022,** *in press*.

726   40.   Jha, N. K.; Al-Yaseri, A.; Ghasemi, M.; Al-Bayati, D.; Lebedev, M.; Sarmadivaleh,

727   M., Pore scale investigation of hydrogen injection in sandstone via X-ray micro-tomography.

728   *Int J Hydrog Energy* **2021,** *46*, 34822-34829.

729   41.   Pak, T.; Butler, I. B.; Geiger, S.; van Dijke, M. I. J.; Sorbie, K. S., Droplet

730   fragmentation: 3D imaging of a previously unidentified pore-scale process during multiphase

731   flow in porous media. *P Natl Acad Sci USA* **2015,** *112* (7), 1947-1952.

732   42.   Iglauer, S.; Ferno, M. A.; Shearing, P.; Blunt, M. J., Comparison of residual oil

733   cluster size distribution, morphology and saturation in oil-wet and water-wet sandstone. *J*

734   *Colloid Interf Sci* **2012,** *375*, 187-192.

735   43.   Iglauer, S.; Paluszny, A.; Blunt, M. J., Simultaneous oil recovery and residual gas

736   storage: A pore-level analysis using in situ X-ray micro-tomography. *Fuel* **2013**, *103*, 905-

737   914.

738   44.   Pentland, C. H.; Tanino, Y.; Iglauer, S.; Blunt, M. J., Capillary trapping in water-wet

739   sandstones: coreflooding experiments and pore-network modeling. In *SPE International*

740   Society of Petroleum Engineers Florence, Italy 2010.

741   45.   Fusseis, F.; Steeb, H.; Xiao, X.; Zhu, W.-l.; Butler, I. B.; Elphick, S.; Maeder, U.,

742   A low-cost X-ray-transparent experimental cell for synchrotron-based X-ray

743   microtomography studies under geological reservoir condition. *J Synchrotron Radiation* **2014**

744   *21* (1), 251-253.

745   46.   Pak, T. Saturation tracking and identification of residual oil saturation. University of

746   Edinburgh 2014.

747   47.   Kumar, M.; Sok, R.; Knackstedt, M. A.; Latham, S.; Senden, T. J.; Sheppard, A.

748   P.; Varslot, T.; Arns, C. In *Mapping fluid distributions in 3D at the pore scale: Quantifying*

749   *the influence of wettability and saturation*

750   *history on rock resistivity*, SPWLA 50th Annual Logging Symposium, Society of

751   Petrophysicists and Well-Log Analysts: 2009.

752   48.   Yusibani, E.; Nagahama, Y.; Kohno, M.; Takata, Y.; Woodfield, P. L.; Shinzato,

753   K.; Fujii, M., A capillary tube viscometer designed for measurements of hydrogen gas

754   viscosity at high pressure and high temperature. *Int J Thermophys* **2011,** *32* (6), 1111-1124.

755   49.   Chow, Y. T. F.; Maitland, G. C.; Trusler, J. P. M., Interfacial tensions of (H_2O + H-

756   2) and (H_2O + CO_2 + H-2) systems at temperatures of (298-448) K and pressures up to 45

757   MPa. *Fluid Phase Equilibr* **2018,** *475*, 37-44.

758   50.   Chow, Y. T. F.; Maitland, G. C.; Trusler, J. P. M., Erratum to "Interfacial tensions of

759   (H_2O + H-2) and (H_2O + CO_2 + H-2) systems at temperatures of (298-448) K and pressures

760   up to 45 MPa". *Fluid Phase Equilibr* **2020,** *503* (112315), 1.

761   51.   Nakai, T.; Sawamura, S.; Taniguchi, Y.; Yamaura, Y., Effect of pressure on the

762   viscosity B coefficient of cesium chloride in water *Mater Sci Res Int* **1996,** *2* (3), 143-147.

763   52.   Vlassenbroeck, J.; Masschaele, B.; Cnuddle, V.; Dierick, M.; Pieters, K.; Van

764   Hoorebeke, L.; Jacobs, P., Octopus 8: A high performance tomographic reconstruction

765   package for X-ray tube and synchrotron micro-CT. In *Advances in X-ray tomography for*

766   *geomaterials*, Desrues, J.; Viggiani, G.; Bésuelle, P., Eds. ISTE: London, UK, 2010.

767   53.   Buades, A.; Coll, B.; Morel, J. M. In *A non-local algorithm for image denoising*,

768   2005 IEEE Computer Society Conference on Computer Vision and Pattern Recognition

769   (CVPR'05), 2005; pp 60-65.

770   54.   Blunt, M. J., *Multiphase flow in permeable media. A Pore-scale perspective*

771   Cambridge University Press Cambridge, United Kingdom, 2017.

772   55.   Singh, K.; Menke, H.; Andrew, M.; Lin, Q.; Rau, C.; Blunt, M. J.; Bijeljic, B.,

773   Dynamics of snap-off and porefilling events during two-phase fluid flow in permeable media.

774   *Sci Rep* **2017,** *7* (5192), 1-13.

775   56.   Roof, J. G., Snap-off of oil droplets in water-wet pores. *Soc Petrol Eng J* **1970,** *10* (1),

776   85-90.

777   57.   Thomas, L. K.; Katz, D. L.; Tek, M. R., Threshold pressure phenomena in porous

778   media. *Soc Petrol Eng J* **1968**, 174-184.

779   58.   Boone, M. A.; Kock, T. D.; Bultreys, T.; Schutter, G. D.; Vontobel, P.; Hoorebeke,

780   L. V.; Cnudde, V., 3D mapping of water in oolithic limestone at atmospheric and vacuum

781   saturation using X-ray micro-CT differential imaging. *Mater Char* **2014,** *97*, 150-160.

782   59.   De Lucia, M.; Pilz, P.; Liebscher, A.; Kuhn, M., Measurements of H2 solubility in

783   saline solutions under reservoir conditions: preliminary results from project H2STORE.

784   *Enrgy Proced* **2015,** *76*, 487-494.

785   60.   Herring, A. L.; Harper, E.; Andersson, L.; Sheppard, A.; Bay, B. K.; Wildenschild,

786   D., Effect of fluid topology on residual nonwetting phase trapping: Implications for geologic

787   CO_2 sequestration. *Adv Water Resour* **2013,** *62*, 47-58.

788   61.   Hassanpouryouzband, A.; Joonaki, E.; Edlmann, K.; Haszeldine, R. S., Offshore

789   Geological Storage of Hydrogen: Is This Our Best Option to Achieve Net-Zero? *ACS Energy*

790   *Lett* **2021,** *6* (6), 2181–2186.

791   62.   Wagner, O. R.; Leach, R. O., Effect of interfacial tension on displacement efficiency.

792   *SPE J* **1966,** *6* (4), 335-344.

793   63.   Avraam, D. G.; Payatakes, A. C., Flow Mechanisms, Relative Permeabilities, and

794   Coupling Effects in Steady-State Two-Phase Flow through Porous Media. The Case of

795   Strong Wettability. *Ind Eng Chem Res* **1999,** *38*, 778-786.

796   64.   Cho, J.; Kim, T. H.; Chang, N.; Lee, K. S., Effects of relative permeability change

797   resulting from interfacial tension reduction on vertical sweep efficiency during the CO2-LPG

798   hybrid EOR process. *Energy Sources* **2018,** *40* (10), 1242-1249.

799   65.   Sabet, N.; Hassanzadeh, H.; Abedi, J., Stability of Gravitationally Unstable Double

800   Diffusive Transient Boundary Layers with Variable Viscosity in Porous Media. *Aiche J* **2017,**

801   *63* (6), 2471-2482.

802   66.   Oughanem, R.; Youssef, S.; Peysson, Y.; Bazin, B.; Maire, E.; Vizika, O., Pore-

803   scale to core-scale study of capillay desaturation curves ulti multi-scale 3D imaging In

804   *International Symposium of the Society of Core Analysts*, Napa Valley, California, USA,

805   2013.

806   67.   Ding, M.; Kantzas, A., Capillary number correlations for gas-liquid systems. *J Can*

807   *Petrol Technol* **2007,** *46* (27-32).

808

809

Supplementary Information

Pore-scale imaging of hydrogen displacement and trapping in porous media

Eike M. Thaysen[2*], Ian Butler[1], Damien Freitas[1], Aliakbar Hassanpouryouzband[1], Fernando Alvarez-Borges[2], Samuel C. Krevor[3], Niklas Heinemann[1], Robert Atwood[2], Katriona Edlmann[1]

[1]School of Geoscience, Grant Institute, The King's Buildings, The University of Edinburgh, James Hutton Road, Edinburgh, EH9 3FE, United Kingdom

[2] Diamond Light Source Ltd, Harwell Campus, Didcot OX11 0DE, UK

[3] Department of Earth Science and Engineering, Imperial College London, London SW7 2AZ, United Kingdom
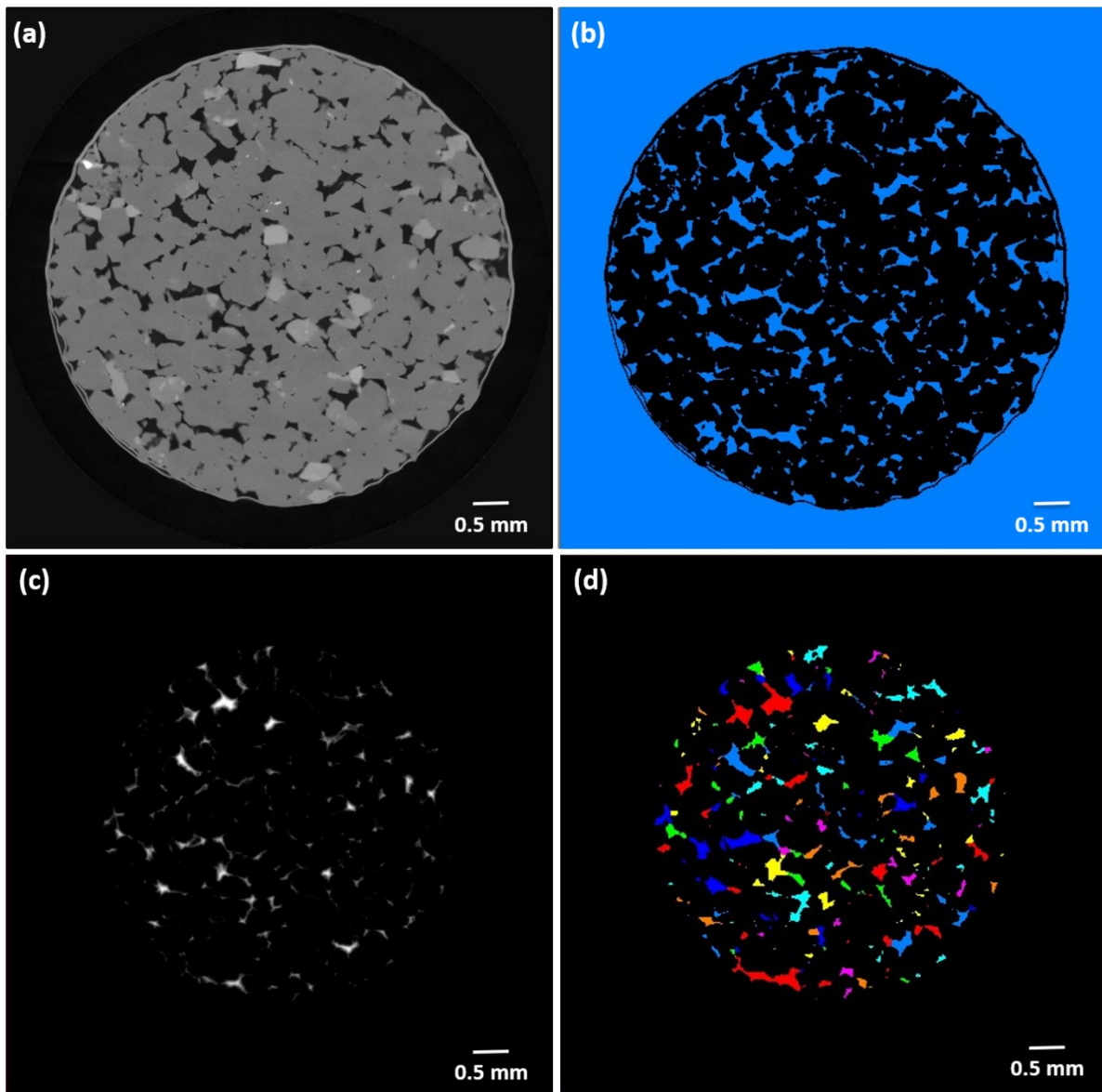
823
824   SI Figure S1: Image processing workflow for UoE experiments. **(a)** The image after reconstruction and filtering.
825   **(b)** The image after segmenting using a global threshold. **(c)** The outer part of the rock core touching the Al foil
826   was removed through application of a mask, and a chamfer distance map of the pore space was calculated by
827   assigning each voxel the distance from it to the nearest pore wall. **(d)** This was then used to separate the pore
828   space into individual pores by calculating the water-shed basins of the distance map.

829
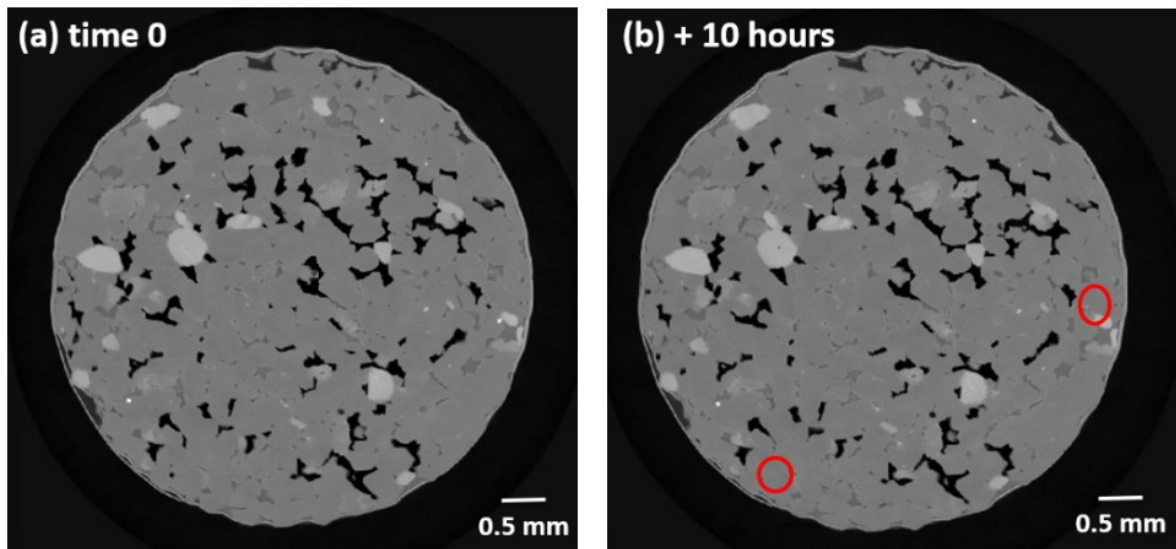
SI Figure S2: H$_2$ stability at 7 MPa injection pressure and a flow rate of 20 µl min^{-1} (capillary number 2*10^{-8}) at time zero **(a)** and after ten hours **(b)**. Red circles indicate subtle differences in the hydrogen filled pore volume after ten hours. The difference in the hydrogen saturation for the total scanned rock volume was within error at 49.55% % and 49.53% for time 0 and after ten hours, respectively.
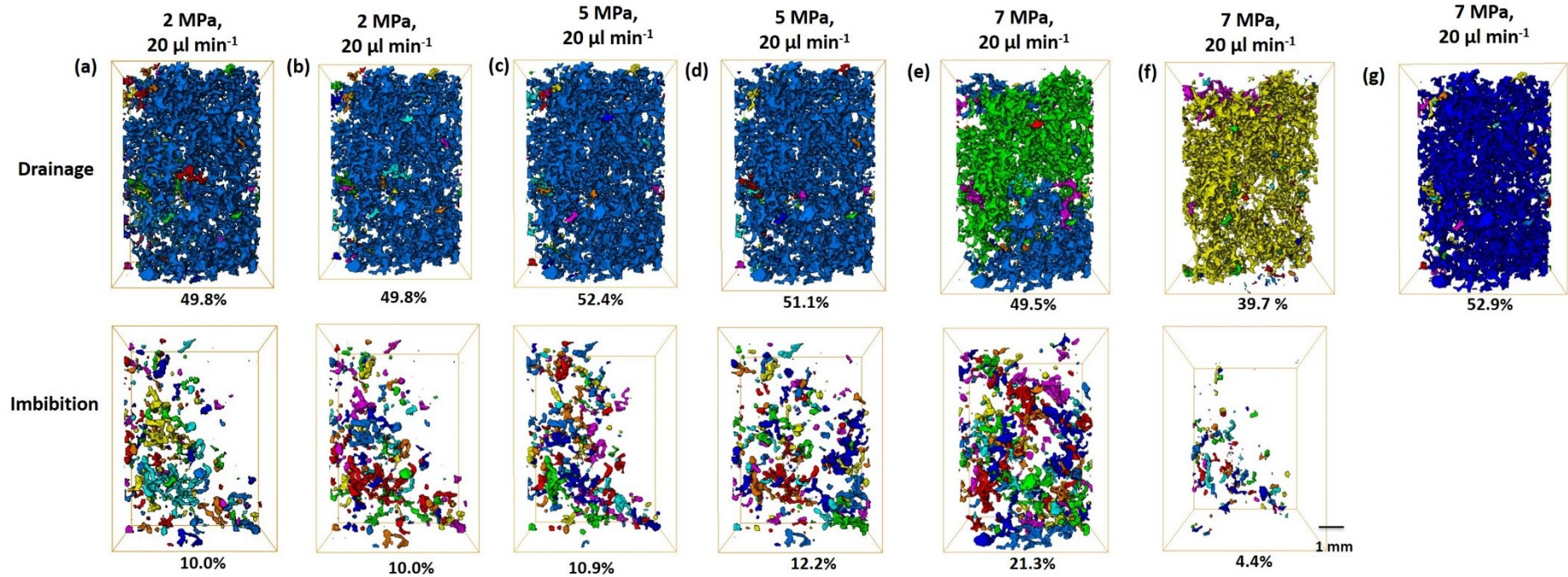
SI Figure S3: Enlarged view of 3D renderings of H_2 with saturation percentages in UoE experiments. Discrete clusters were rendered in colours, where mainly one colour marks one large, connected cluster and different colours indicate several, not connected clusters. **(a-d)** Effect of pore fluid pressure on H_2 clusters and saturation after drainage and after primary imbibition. **(a)** 2 MPa, **(b)** 5 MPa and **(c-e)** 7 MPa, all at a constant flow rate of 20 µl min^{-1} corresponding to capillary numbers of 1.7×10^{-8} and 2.4×10^{-6}, respectively.. Experiments were repeated once. For experiments at 2 MPa and 5 MPa averages and standard errors for the H_2 saturation are reported. For experiments at 7 MPa, due to the discrepancy in the results, both results are visualized **(c-d)**.
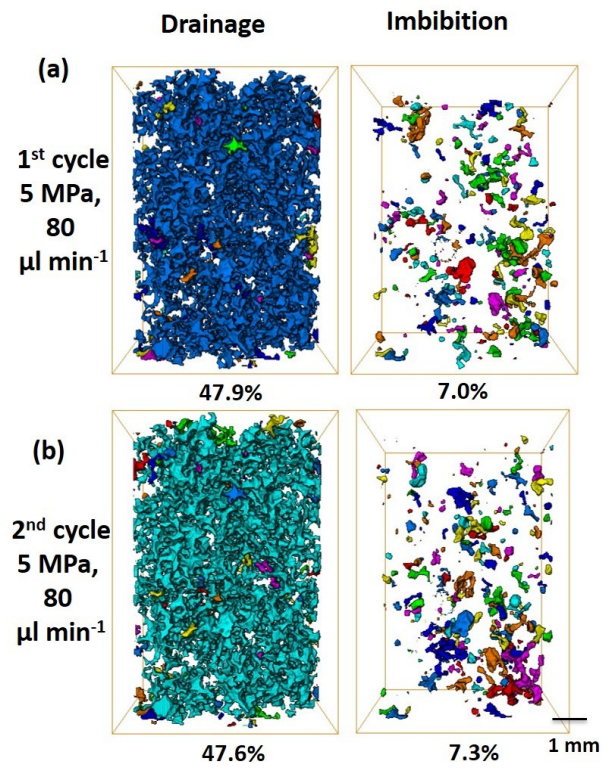
SI Figure S4: Cyclic H_2 injection into Clashach sandstone at 5 MPa and 80 µl min^{-1} corresponding to a capillary number of 9.4×10^{-6}, showing no significant differences in H_2 saturation and H_2 connectivity after primary drainage and imbibition as compared to after secondary drainage and imbibition.
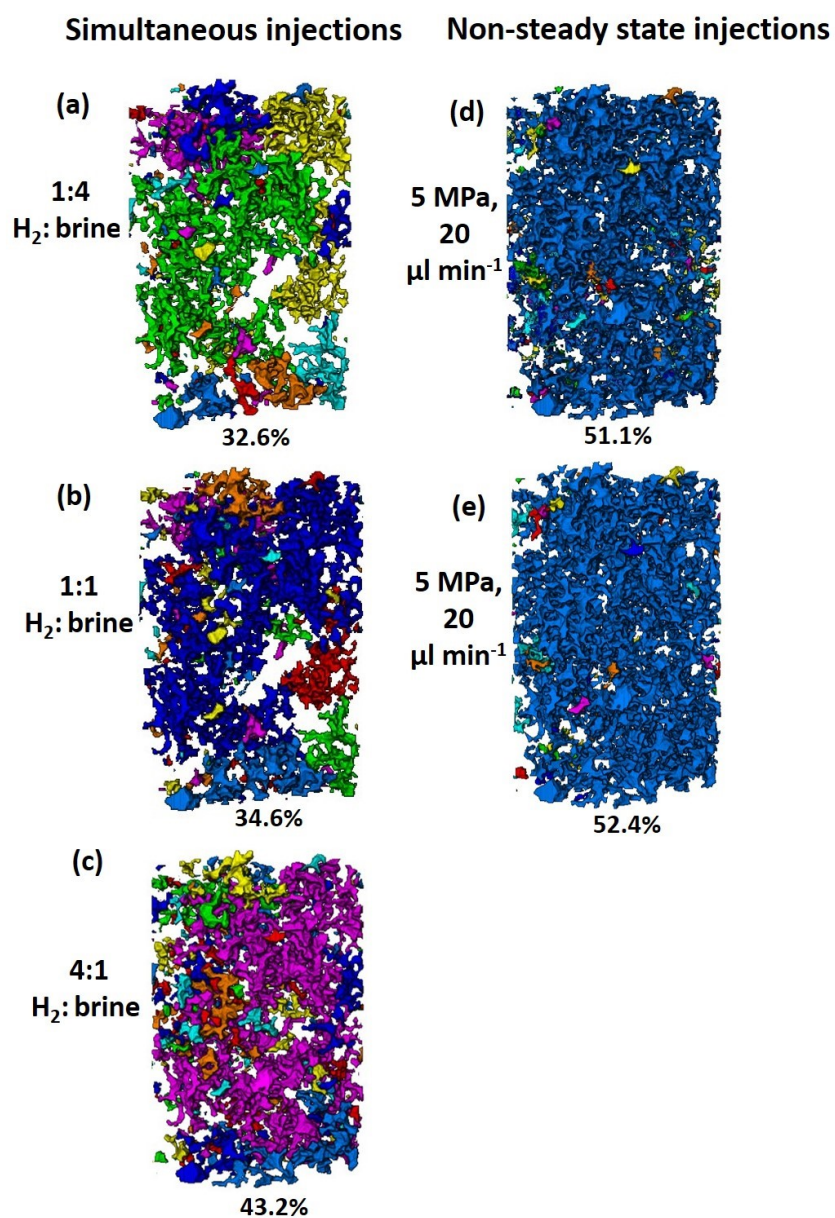
SI Figure S5: Comparison of the distribution of the H_2 clusters in the pore space between simultaneous H_2 and brine injection experiments **(a-c)** and the two repetitions of the non-steady state H_2 injection **(d)** and **(e)**, all at 5 MPa and a total flow rate of 20 µl min^{-1}.

Drainage **Imbibition** **Drainage** **Imbibition**

(a) **(b)**

H$_2$, 5 MPa, 20 µl min^{-1}

N$_2$, 5 MPa, 20 µl min^{-1}

51.7 ±0.66%   11.5 ± 0.64%   1 mm

48.7%   33.9%   1 mm
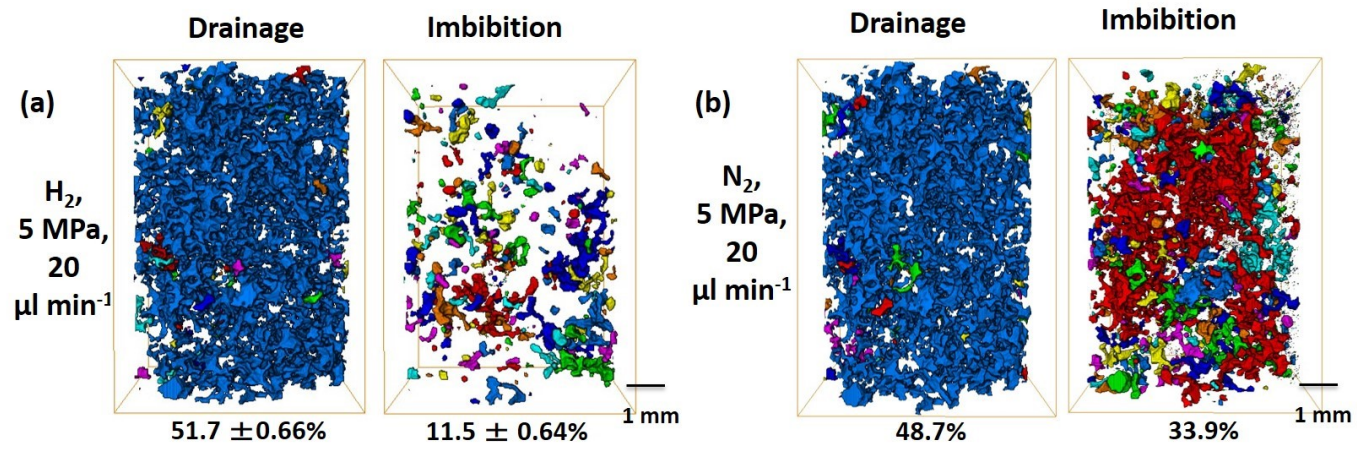
SI Figure S6: Nitrogen clusters and saturations during drainage and imbibition at 5 MPa pore fluid pressure and a flowrate of 20 µl min^{-1}